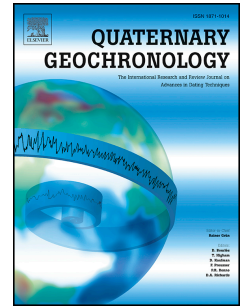# Accepted Manuscript

Investigation of OSL surface exposure dating to reconstruct post-LIA glacier fluctuation in the French Alps (Mer de Glace, Mont Blanc massif)

Benjamin Lehmann, Pierre G. Valla, Georgina E. King, Frédéric Herman

Please cite this article as: Lehmann, B., Valla, P.G., King, G.E., Herman, Fréé., Investigation of OSL surface exposure dating to reconstruct post-LIA glacier fluctuation in the French Alps (Mer de Glace, Mont Blanc massif), *Quaternary Geochronology* (2018), doi: 10.1016/j.quageo.2017.12.002.

1 Investigation of OSL surface exposure dating to reconstruct post-LIA

2 glacier fluctuation in the French Alps (Mer de Glace, Mont Blanc massif)

3 Benjamin Lehmann[1], Pierre G. Valla[1,2], Georgina E. King[1,2] and Frédéric Herman[1]

4 [1] Institute of Earth Surface Dynamics, University of Lausanne, Lausanne, 1012, Switzerland
5 [2] Institute of Geological Sciences and Oeschger Centre for Climate Change Research, University of
6 Bern, Bern, 3012, Switzerland
7
8 *Correspondence to*: Benjamin Lehmann (benjamin.lehmann@unil.ch)
9

10 **Abstract**

11 Providing quantitative constraints on late Pleistocene glacier fluctuations remains an important

12 challenge for understanding glacier response to past and future climate changes. In most mountainous

13 settings, paleo-glacier reconstructions are limited because they often lack precise temporal constraint.

14 Different geochronological methods have been developed and applied to date specific

15 geomorphological or sedimentological markers for paleo-glacier dynamics. Recently, OSL (optically

16 stimulated luminescence) surface exposure dating has been introduced and provides us with an

17 opportunity to improve paleo-glacier reconstructions. This method is based on the sensitivity of the

18 OSL signal from rock minerals to light, resulting in bleaching of the OSL signal within the upper first

19 millimeters of the exposed rock surface, a process that depends on the exposure age, the rock type and

20 the local setting (e.g. topographic shielding, bedrock orientation etc.). Here, we investigate the

21 potential of OSL surface exposure along a vertical cross-section of polished bedrock surfaces with

22 known post-LIA (Little Ice Age) exposure ages (from 3 to 137 years) along the Mer de Glace glacier

23 (Mont Blanc massif, France). The infra-red stimulated luminescence (IRSL) signals from rock slices

24 exhibit increasingly deep bleaching profiles with elevation and thus exposure age, which is consistent

25 with progressive glacier thinning since the LIA. Our results show that OSL surface exposure dating

26 can be applied to periglacial environments, and is a promising tool for high-resolution reconstruction

27 of ice-extent fluctuations, both in space and time.

28

29 **Keywords**: Optically stimulated luminescence (OSL), surface exposure dating, luminescence depth

30 profile, paleo-glacier reconstruction, Mont Blanc massif

31 **1. Introduction**

32 During the last ca. 5 Ma of the Earth's history, global climate cooled and evolved towards oscillating

33 climatic conditions that intensified towards the present (e.g. Zachos et al., 2001; Herbert et al., 2016).

34 This climate shift left a strong imprint on mountain topography (e.g. Penck, 1905; Broecker and

35 Denton, 1990; Molnar and Engand, 1990; Peizhen et al., 2001; Egholm et al., 2009). However,

36 understanding paleo-climatic conditions in mountainous areas over the Plio-Pleistocene epochs

37 remains difficult. Local records of successive glacial/interglacial cycles are scarce or poorly preserved

38 over such long timescales (Ehlers and Gibbard, 2007). Polar ice-sheets and marine cores are useful for

39 providing long-term global climatic records but are unable to describe regional continental climate. In

40 contrast, glaciers and their fluctuations through time provide invaluable information on past mountain

41 climatic conditions. Through mapping and dating moraine deposits and erratic boulders, it is possible

42 to reconstruct the history of ice-extent (e.g. for the European Alps: Ivy-Ochs et al., 2006; Bini et al.,

43 2009; Preusser et al., 2011; Schimmelpfennig et al. 2014; Ivy-Ochs et al., 2015; Wirsig et al., 2016).

44   Past glacier extents in the European Alps are well constrained since the Little Ice Age (LIA:

45 15th to 19th centuries). Using historical maps, survey reports and aerial photogrammetry, glacier

46 fluctuations have been precisely reconstructed over the last two centuries (e.g. Vincent et al., 2014).

47 To go further back in time into the Pleistocene, different geochronological methods can be used such

48 as lichenometry (Winkler et al., 2004), varve chronologies (Stewart et al., 2011), dendrochronology

49 (Baillie, 1995) and radiocarbon dating (Hajdas, 2008). However, organic matter can be scarce for

50 glacial/periglacial deposits because of extremely active geomorphic systems associated with glacial

51 environments. In addition to these methods, surface exposure dating of polished bedrock or erratic

52 boulders using terrestrial *in situ* cosmogenic nuclides has been developed over the last decades (Lal et

53 al., 1991; Gosse and Philips, 2001; Balco, 2011; Ivy-Ochs and Briner, 2014), and has been widely

54 used in the European Alps (see Ivy-Ochs et al., 2006; 2009 for reviews). The combination of different

55 cosmogenic nuclide pairs (e.g. ^{10}Be and ^{14}C: e.g. Goehring et al., 2012; Hippe et al., 2014) provides us

56 with important information on Alpine glacier paleogeography since the Last Glacial Maximum (LGM;

57 Ivy-Ochs et al., 2006; Wirsig et al., 2016). However, the cosmogenic nuclide production rate and the

58 integration of production over the first 1-2 meters below a rock surface may limit the resolution of

59 such methods for recent and/or complex exposure histories.

60   Here we investigate whether optically stimulated luminescence (OSL) surface exposure dating

61 can be used to reconstruct recent glacier fluctuation. Luminescence dating is based on the

62 accumulation of trapped electrons through time in the crystalline lattice of certain minerals (e.g. quartz

63 or feldspar). Some of these trapped electrons are sensitive to daylight exposure (Aitken, 1985; Huntley

64 et al., 1985). Luminescence dating is commonly used to date sediment burial in a range of

65 geomorphological environments (e.g. Duller, 2008; Rhodes, 2011; Fuchs and Owen, 2008) but can

66 also be used to determine rates of bedrock cooling (Guralnik et al., 2015; King et al., 2016; Brown et

67 al., 2017), and the exposure age of archaeological rock surfaces (Polikreti et al., 2003; Sohbati et al.,

68 2011). This latter application is based on the principle that when a rock surface is exposed to light, the

69 luminescence signal, which is initially homogenous within the rock sample (at a given level or in field

70 steady-state; e.g. Valla et al., 2016), will progressively decrease at depth until being completely

71 zeroed, a phenomenon called "bleaching" (Aitken, 1998). The assumption used in this study is that the

72 longer a surface has been exposed to daylight, the deeper the signal bleaching will be (Polikreti et al.,

73 2002). In granitic and gneissic rocks, bleaching through time has been shown to occur over the first

74 few centimetres depth of the rock surface (Vafiadou et al., 2007; Sohbati et al., 2011; Freiesleben et

75 al., 2015). In alpine environments, glacier advances during the late Pleistocene to Holocene have been

76 associated with subglacial erosion of bedrock at the centimetre-scale (e.g. Goehring et al., 2011). This

77 means that only the most recent exposure history of the bedrock will be recorded, as earlier exposure

78 histories and OSL bleaching evidence will have been eroded by subsequent glacier advances. OSL

79 surface exposure dating would thus in theory enable past glacier extents to be reconstructed with a

80 high temporal resolution for both recent and complex exposure histories. Furthermore, this method is

81 attractive because of the short time required for sample preparation (Sohbati et al., 2011), although

82 one current disadvantage is the requirement for calibration of this chronometer on rock surfaces with

83 independently known exposure ages (Sohbati et al., 2012a).

84   In the following, we first introduce the study site, i.e., the Mer de Glace, and our sampling

85 strategy. We have targeted several independently dated glacially eroded bedrock surfaces, which

86 represent past elevations of the glacier surface since the LIA. We then review the basic principles of

87 the method and present the luminescence signals for six different surfaces along a vertical cross

88 section above the present-day Mer de Glace. Our results show a strong correlation between sample

89 elevation, exposure age and bleaching depth. Finally, we use this dataset to show that model

90 calibration requires multiple samples of known age to take full advantage of OSL surface exposure

91 dating in both glaciated and formerly glaciated environments.

92 **2. Setting and sampling strategy**

93 **2.1. Geomorphological setting**

94 The Mer de Glace glacier (Fig. 1) is about 11.5 km long and is located in the Mont Blanc massif. The

95 modern glacier covers an area of 30.4 km^2 (excluding former tributary Talèfre Glacier) and spans an

96 elevation range from 4205 m to 1531 m.a.s.l. (data from 2008; Gardent et al., 2014). The mean

97 equilibrium line altitude (ELA), reconstructed using remote sensing methods, was about 2880 m.a.s.l.

98 between 1961 and 1990 for five of the main north-facing Mont Blanc massif glaciers, including the

99 Leschaux Glacier for the period 1984-2010 (Rabatel et al., 2013).

100   The Mer de Glace is an appropriate laboratory for validating the application of OSL surface

101 exposure dating for paleo-glacier reconstruction. Numerous studies have provided detailed

102 reconstructions of Mer de Glace fluctuations from the LGM towards the Holocene and present day

103 (Coutterand and Buoncristiani, 2006; Nussbaumer et al, 2007; Vincent et al., 2014; LeRoy et al.,

104 2015). The Montenvers site (Fig. 1) was chosen as an optimal study site as the evolution of the glacier

105 thickness since the LIA has been reconstructed by Vincent et al. (2014) using historical maps, aerial

106 photogrammetry and satellite-derived digital elevation models (see Section 2.3 for details).

107 Furthermore, the rock type is generally homogenous along the valley flank (i.e. orthogneiss; Dobmeier

108   et al., 1998), avoiding any lithological dependency of the OSL surface exposure dating approach

109   although occasional granitic lenses are exposed in the lower part of the profile (see Section 2.2 for

110   details).

111   Our sampling strategy was to collect glacially polished bedrock surfaces with the best-

112   preserved erosion patterns (glacial striations, roches moutonnées; Fig. 3) to ensure that sample

113   bleaching profiles reflect the period of time since post-LIA deglaciation. The samples were also

114   selected to have low topographic shielding and vegetation cover (e.g. lichen). Steep slopes were

115   selected (i.e. above 30°) to limit any potential snow cover effects. In particular, we focused on rock

116   surfaces exhibiting striations parallel to the Mer de Glace flow line in order to avoid the potential

117   influence of tributary glaciers.

118
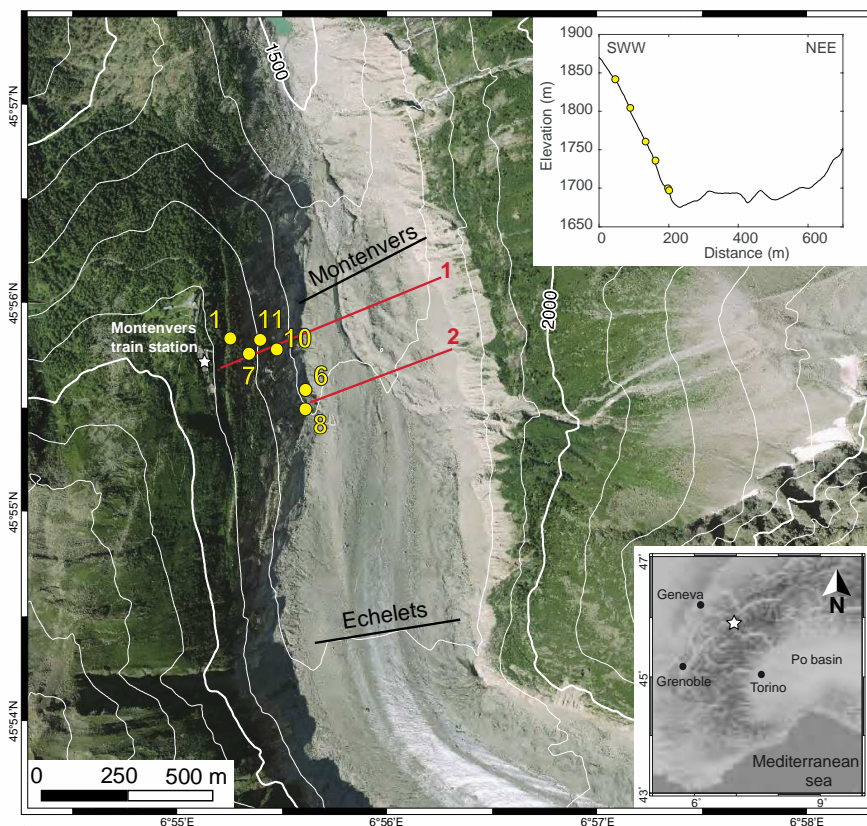
119
120   **Figure 1:** Sampling map of the Montenvers site, Mer de Glace. The orthorectified aerial photograph

121   of the Mer de Glace was acquired in 2016 (source: www.geoportail.gouv.fr). The black lines show the

122   two cross-sections produced by Vincent et al. (2014) which we interpolated to reconstruct glacier

123   surface elevations at two different locations (red lines 1 and 2, see Section 2.3 and Supplementary Fig.

124   A1) where samples were collected (yellow dots with numbers). Upper right inset represents the

125   collected samples projected along cross-section 1. Bottom right inset shows location of the study area

126   within the western Alps.

4

2.2 Sample description

We collected six samples along the Montenvers profile during several field campaigns (2015-2016), ranging in elevation from 1841 to 1696 m.a.s.l. (Fig. 1 and Table 1). Samples MBMV1, MBMV7, MBMV8, MBMV10 and MBMV11 consist of coarse-grained orthogneiss, typical for the Aiguilles Rouges massif (Dobmeier et al., 1998). These rocks mainly comprise coarse K-feldspar crystals, quartz, biotite and muscovite. Only MBMV6 was collected from a granitic lens, which consists of bigger quartz and feldspar crystals than the orthogneiss (Fig. 3b). Because differences in crystals properties may influence light penetration, i.e. due to both crystal size and distribution, sample MBMV6 is used to explore any potential lithological effect on the OSL surface exposure dating approach.
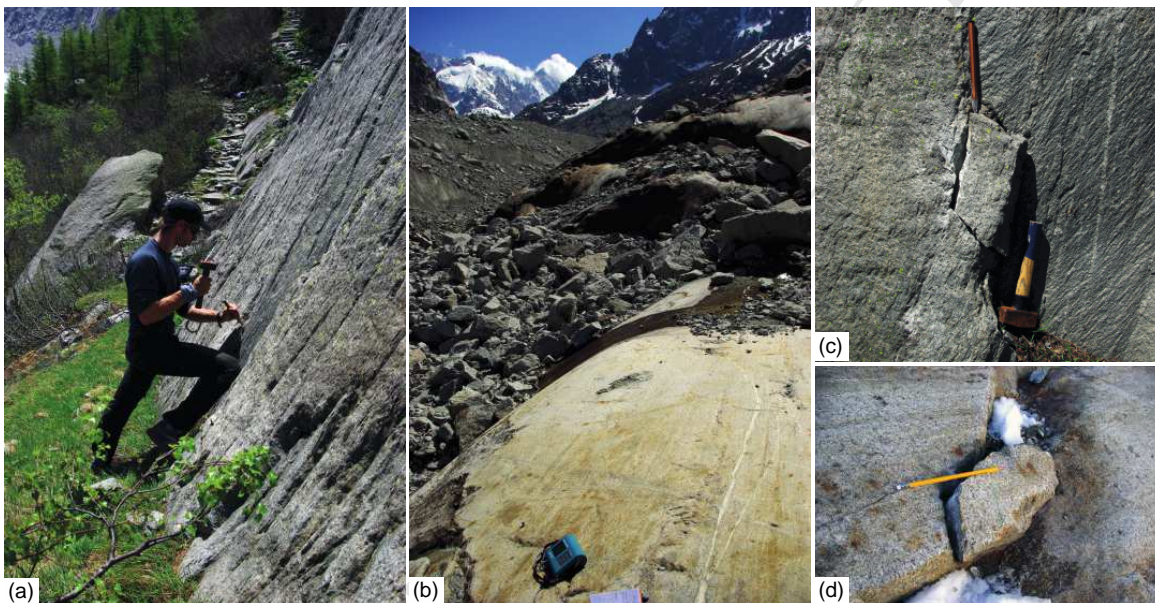

Figure 2: Sampling sites and sample details at the Montenvers site. (a-b) Sampling sites for MBMV7 and MBMV6. (c-d) Outcrops and samples MBMV7 and MBMV6.

Table 1: Sample characteristics from the Montenvers cross-section. Estimated exposure ages were reconstructed using differential GPS and ice-thickness reconstruction as shown in section 2.3. Shielding factors were calculated with the geometric shielding calculator (CRONUS-Earth project). Note that all estimated exposure ages are referenced from 2015 (date of the first field campaign).

Sample ID	Latitude	Longitude	Elevation	Lithology	Estimated Exposure Age	Topographic	Surface
	WGS 84		[m.a.s.l.]		[Year before 2015]	shielding factor	orientation
MBMV1	45°55'54.0''	06°55'07.7''	1841	Gneiss	137	0.81	N8 55°E
MBMV6	45°55'48.9''	06°55'17.7''	1696	Granite	2	0.92	N0 30°E
MBMV7	45°55'52.7''	06°55'09.9''	1804	Gneiss	69	0.79	N374 60°E
MBMV8	45°55'47.7''	06°55'18.5''	1699	Gneiss	3	0.81	N13 54°E
MBMV10	45°55'54.0''	06°55'14.1''	1735	Gneiss	18	0.79	N0 60°E
MBMV11	45°55'54.3''	06°55'11.5''	1760	Gneiss	30	0.88	N355 75°E

145

146
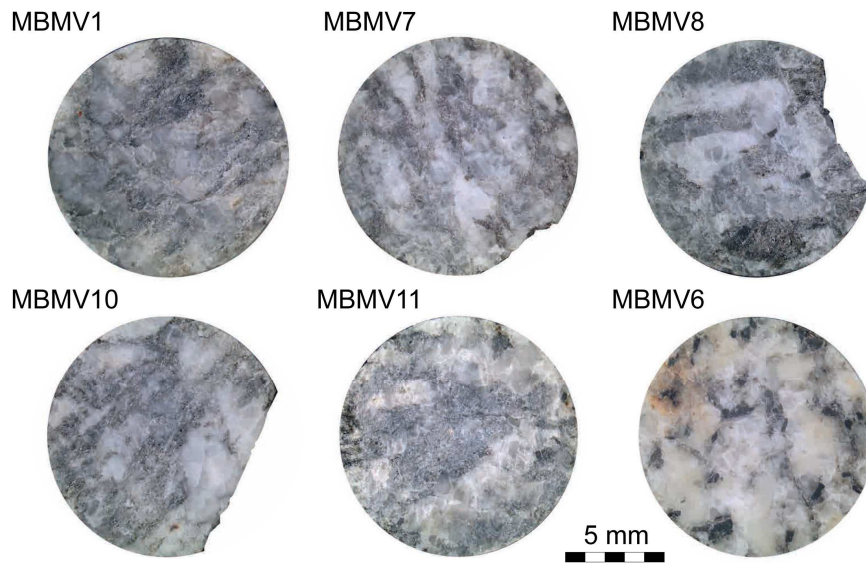
Figure 3: Pictures of selected rock slices (see section 3.1 for details), showing the difference in composition and texture between orthogneiss (MBMV1, MBMV7, MBMV8, MBMV10, and MBMV11) and granite (MBMV6).

2.3 Independent age calibration from glacier thickness reconstruction

We use the historical post-LIA reconstruction of the Mer de Glace thickness (Vincent et al., 2014) available for two cross-sections: Montenvers and Echelets (Fig. 1). Samples MBMV1, MBMV7, MBMV10 and MBMV11 were collected from the same profile located 290 m upstream of the Montenvers cross-section and 690 m downstream of the Echelets cross-section (cross-section 1, Figs. 1 and 4). Samples MBMV6 and MBMV8 were taken along a profile (cross-section 2, Fig. 1) located 200 m upstream of the cross-section 1. Because glacial thinning would progressively expose bedrock surfaces at lower elevations, we can use the relationship between exposure age and sample elevation to constrain the temporal evolution of glacial thickness (Fig. 1 and 4).

Post-LIA thickness reconstructions of the Mer de Glace for cross-sections 1 and 2 have been interpolated from the Montenvers and Echelets cross-sections. Exposure ages from 2 to 137 years were obtained for the different samples, using either cross-section 1 (MBMV1, MBV7, MBMV10 and MBMV11) or cross-section 2 (MBMV6 and MBMV8) (see Supplementary Material A1). All exposure ages are relative to the first sampling campaign in summer 2015.

3. Methodology: OSL surface exposure dating

3.1. Theoretical approach

Minerals such as quartz and feldspar naturally contain defects or impurities in their crystal lattice. Energy released by ambient radiation (i.e. cosmic rays and the flux of high-energy solar particles or/and radioactive decay in the rock-matrix) excites electrons from their equilibrium state (valence band), and these can become trapped at higher energy levels within the crystal. Because of the finite number of traps, electron filling occurs until saturation is reached. By giving energy to the system in the form of light or heat (natural bleaching processes), electrons are released and return to their equilibrium state, producing photons. This phenomenon is called luminescence and the intensity of a given luminescence signal is thus proportional to the number of trapped electrons (Aitken, 1985; 1998). In a rock surface continuously exposed to daylight, the progressive bleaching of the luminescence signal is expected to propagate deeper into the surface with time (Habermann et al., 2000; Polikreti et al., 2002; Laskaris and Liritzis, 2011).

Rock surface dating was first used in archaeology, and was based on thermally-stimulated measurements, i.e. thermoluminescence (TL; Liritzis et al., 1994; Richards et al., 1994; Theocaris et al., 1997; Polikreti et al., 2002; 2003). More recently, optically stimulated luminescence dating (OSL; e.g. Habermann et al. 2000; Vafiadou et al., 2007) has been introduced to date surface exposure, which benefits from improved measurement reproducibility and more rapid signal bleaching following exposure to daylight than typically-used TL signals (e.g. the 325°C TL peak in quartz). The potential of OSL for dating exposure events in geomorphological (Freiesleben et al., 2015; Sohbati et al., 2015) and archaeological (Liritzis, 2011) contexts has recently been investigated, and a range of applications including relative sea-level changes and coastal geomorphology (Simms et al., 2011; Simkims et al., 2013) have been published. However, OSL surface exposure dating has not yet been applied to glacially polished bedrock surfaces.

In mountainous environments, OSL dating can be used to evaluate the exposure age of a polished bedrock surface as described in Figure 4. At the initial condition (t_1 in Fig. 4), the glacier has reached its maximum thickness. Ice and periglacial sediments cover the bedrock surface, and the luminescence signals of bedrock minerals are in field steady-state and uniform in the rock column. When the glacier retreats, freshly-eroded surfaces are exposed to daylight (point **a** at time t_2, Fig. 4). The initial luminescence signals start to bleach for these exposed surfaces, while the sample at lower elevation is still covered by the glacier and its luminescence signals remain uniform in the rock (point **b** at time t_2, Fig. 4). As the glacier continues to thin, the lower part of the bedrock flanks are uncovered (t_3, Fig. 4) and the luminescence signals start to bleach for the lower-elevation surfaces. Therefore, in a setting affected by progressive glacier retreat and thinning, there is a direct correlation between the elevation of the studied site and the exposure age, with the assumption that the longer a surface is

7

200   exposed to daylight, the deeper into the rock the luminescence signal is bleached (Freiesleben et al.,

201   2015; Sohbati et al., 2011).
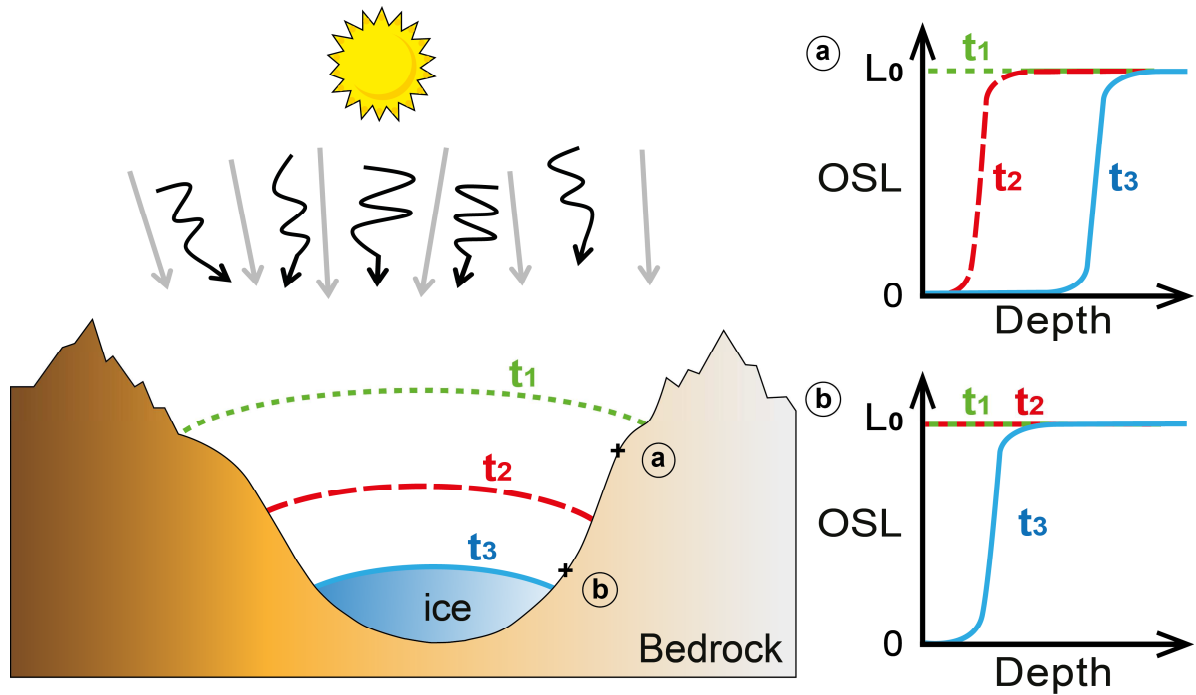
202

203   **Figure 4:** Sketch linking glacier thinning and OSL signal evolution for two bedrock surfaces located

204   at different elevations along the valley flank. Straight arrows (grey) represent cosmic rays and high-

205   energy solar particle flux; this radiation, together with radioactive decay in the rock matrix build up

206   the latent luminescence signal. Other arrows (black) represent low energy electromagnetic radiation

207   from the sun; this radiation bleaches the latent luminescence signal. At the initial time t_1, the glacier is

208   at its maximum extent and the OSL signals for both surfaces are in field steady-state and uniform

209   within the rocks, L_0. At time t_2, the glacier has retreated and exposed the surface (a), the OSL signal

210   begins to bleach whilst surface (b) remains covered with its luminescence signal unchanged. In the

211   final step t_3, the glacier size has shrunk, surface (a) remains exposed and its OSL signal is bleached at

212   greater depth while surface (b) has just been exposed to daylight and its OSL signal has been bleached

213   just below the exposed surface.

214   **3.2. Modelling approach**

215   To assess rock surface exposure durations to daylight from a luminescence depth profile, we use the

216   model proposed by Sohbati et al. (2011; 2012a,b) who provide an in-depth review of each parameter.

217   When a rock surface is exposed to daylight, both detrapping (due to the release of energy by daylight)

218   and trapping (due to absorption of energy from ambient radiation) occur simultaneously. The trapped-

219   charge concentration during light exposure is given by the following differential equation:

220

221     $\frac{\partial n(x,t)}{\partial t} = -E(x)\, n(x,t) + F(x)\, [N(x) - n(x,t)]$ (1)

222

223   Where $n(x,t)$ is the trapped charge concentration [m^{-3}] at time t [s] and depth x [m], $N(x)$ is the

224   concentration of sites [m^{-3}] available for trapping at depth x, $E(x)$ is the charge detrapping rate [s^{-1}],

225   and $F(x)$ is the trap filling rate [s^{-1}]. The charge detrapping rate, $E(x)$, is itself given by:

226

227    $E(x) = \overline{\sigma\varphi}_0 \, e^{-\mu x}$ (2)

228

229   where $\varphi_0(\lambda, x)$ is the photon flux [cm^{-2} s^{-1}] describing the rate of incoming photons that can bleach the

230   trap of interest. $\sigma(\lambda)$ is the photoionization cross section [cm^2] describing the probability of this

231   specific trap to be excited by light stimulation. It is averaged over the wavelengths present in the solar

232   spectrum at the surface ($x = 0$). Here, we assume that the photon flux does not fluctuate through time,

233   and we are only concerned with the product of the two parameters, which is given by $\overline{\sigma\varphi}_0$ [s^{-1}] (i.e. the

234   effective decay rate of luminescence; Sohbati et al., 2011). Equation (2) also includes a decay term for

235   light attenuation with depth. The light attenuation coefficient μ [m^{-1}] describes how deep into the rock

236   a photon will penetrate and affect the luminescence signal. μ is assumed to be independent of

237   wavelength in the spectral range of interest (Sohbati et al., 2011).

238   For surface exposure dating of terrestrial surfaces, the effect of trap filling during daylight exposure

239   over short timescales (i.e. centuries) is often negligible (i.e. $F(x) \approx 0$) (see Supplementary Material

240   A2). The trapped charge population at a given depth (x) can then be approximated by:

241

242    $n(x) = n_0 e^{-E(x)t}$ (3)

243

244   where n_0 is the initial charge population [m^{-3}] assumed to be constant with depth within the rock

245   column prior to bleaching. Assuming that the luminescence signal (L) is proportional to n, Eq. (3)

246   becomes:

247

248    $L = \frac{Lx}{Tx} = L_0 \, e^{-\overline{\sigma\varphi}_0 t} \, e^{-\mu x}$ (4)

249

250   where Lx/Tx is the normalized natural luminescence signal measured at depth x [m] after exposure

251   age t [s]. L_0 is the normalized natural luminescence signal before bleaching (Fig. 4), which is sample

252   dependent and can be constrained in the laboratory.

253   Equation 4 can predict the rock luminescence profiles for different exposure ages, however the

254   mean photon flux φ_0, the photoionization cross-section σ, and the attenuation coefficient μ must first

255   be quantified. φ_0 is mainly controlled by the latitude and the cloudiness; and it is broadly correlated to

256   elevation (Blumthaler et al., 1997). The solar irradiance is fluctuating over decadal timescales (Lean,

257   1987) making the independent determination of the photon flux impossible without knowing the time

258   of exposure. The photoionization cross-section σ is depending on both the mineral and the trap

259   targeted (Bailey, 2004). For samples coming from the same region and from a similar lithology, $\overline{\sigma\varphi}_0$

260   is assumed to be uniform and μ is expected to be of the same order of magnitude between samples, but

261   not necessarily equal.

262   The OSL-depth profile of exposed rock surfaces with independently constrained exposure

263   durations can be used to calibrate the $\overline{\sigma\varphi}_0$ and μ parameters by fitting the luminescence signal

264   bleaching with depth (Singarayer, 2002; Sohbati et al., 2012a). These constrained parameters can then

265   be used to determine the exposure histories of unknown-age surfaces from the same region.

266   Here, our objective is to demonstrate the validity of the proposed model (Eq. 4) on polished

267   bedrock surfaces and to calibrate the model parameters on surfaces with known exposure age. To do

268   so, the unknown $\overline{\sigma\varphi}_0$ and μ parameters are inverted for each sample using a probability density

269   function of the model parameters, given the observed OSL-depth profile data. This includes a least

270   absolute deviation regression $\mathcal{L}_{sample}$ (Eq. 5), in which we randomly prescribed a range of different

271     $\overline{\sigma\varphi}_0$ and μ values. From the residual likelihood $\mathcal{L}_{sample}$ obtained, we select the maximum likelihood

272   values of $\overline{\sigma\varphi}_0$ and μ. The modelled luminescence signals $\left(\frac{Lx}{Tx}\right)_m$ are calculated for each rock slice of a

273   given sample using the known exposure age of each sampling site, giving:

274

275     $$\mathcal{L}_{sample} = \exp\left(-\frac{1}{2a}\sum_{i=1}^{n}\left|\left(\frac{Lx}{Tx}\right)_{obs}^{(i)} - \left(\frac{Lx}{Tx}\right)_m^{(i)}\right|\right) \tag{5}$$

276

277   where n is the number of rock slices per sample, $\left(\frac{Lx}{Tx}\right)_m^{(i)}$ is the luminescence signal calculated using

278   Eq. (4), $\left(\frac{Lx}{Tx}\right)_{obs}^{(i)}$ is experimentally measured for each rock slice i and a is the uncertainty. Given that

279   the scatter of the plateau signal (L_0) for every independent sample is larger than the analytical error,

280   we use the standard deviation around the plateau value L_0 to estimate a. Then, we compute the

281   combined likelihood for a number of samples p using:

282

283     $$\mathcal{L}_{combined} = \prod_{j=1}^{p}\mathcal{L}_{sample(j)} \tag{6}$$

284

285 This approach provides the most likely common values of $\overline{\sigma\varphi}_0$ and μ. Once the parameters of the

286 model are determined as shown above, it is possible to invert the exposure age for other rock surfaces

287 using the constrained $\overline{\sigma\varphi}_0$ and μ values (cf. Eq. (5)).

288

289 **Table 2:** Summary of symbols.

290

Symbol	Unit	Definition
n	m^{-3}	Concentration of trapped charge
x	m	Depth
t	s	Time
N	m^{-3}	Concentration of sites available too trap charge
E	s^{-1}	Charge detrapping rate due to solar radiation
F	s^{-1}	Charge trapping due to ionising radiation
σ	cm^2	Photionisation cross-section
φ	cm^{-2} s^{-1}	Photon flux
$\overline{\sigma\varphi}_0$	s^{-1}	Charge detrapping rate
μ	m^{-1}	Attenuation coefficient
Lx	Counts	Regenerated luminescence signal
Tx	Counts	Test dose signal
L	Counts	Luminescence

291

292   In order to verify our modelling approach, we show a synthetic inversion. We produce a

293 synthetic luminescence signal (Lx/Tx for depths in between 0 and 14 mm) using Eq. (4) and sample-

294 specific $\overline{\sigma\varphi}_0$ and μ parameters (obtained from initially fitting every sample using their independent

295 age control, see Section 5.2 for details) and assuming a constant μ value (i.e. homogenous lithology

296 with rock depth). The first step of the synthetic test is to invert parameters $\overline{\sigma\varphi}_0$ and μ knowing the

297 exposure age t for each individual sample as presented above. Then, using these $\overline{\sigma\varphi}_0$ and μ

298 parameters, we subsequently invert for the exposure age t using Eq. (4). In order to study the effect of

299 potential uncertainties from the experimental data on the exposure age determination, we reproduce

300 this synthetic test with white noise on the luminescence signal, with four different amplitudes between

301 0 and 100 % (Fig. 5). Our synthetic results show that our inversion approach can recover the exposure

302 age with 0 to 50% noise. The synthetic test with 100% noise on the luminescence signal provided age

303 outcomes with larger uncertainties (>20%). The best results are obtained using the best-fit of $\overline{\sigma\varphi}_0$ and

304 μ and the median value of the predicted exposure ages. The resulting uncertainties are correlated with

305 the magnitude of the noise, however any potential variability in the luminescence signal does not

306 appear to produce a significant bias on the inverted exposure age.

307
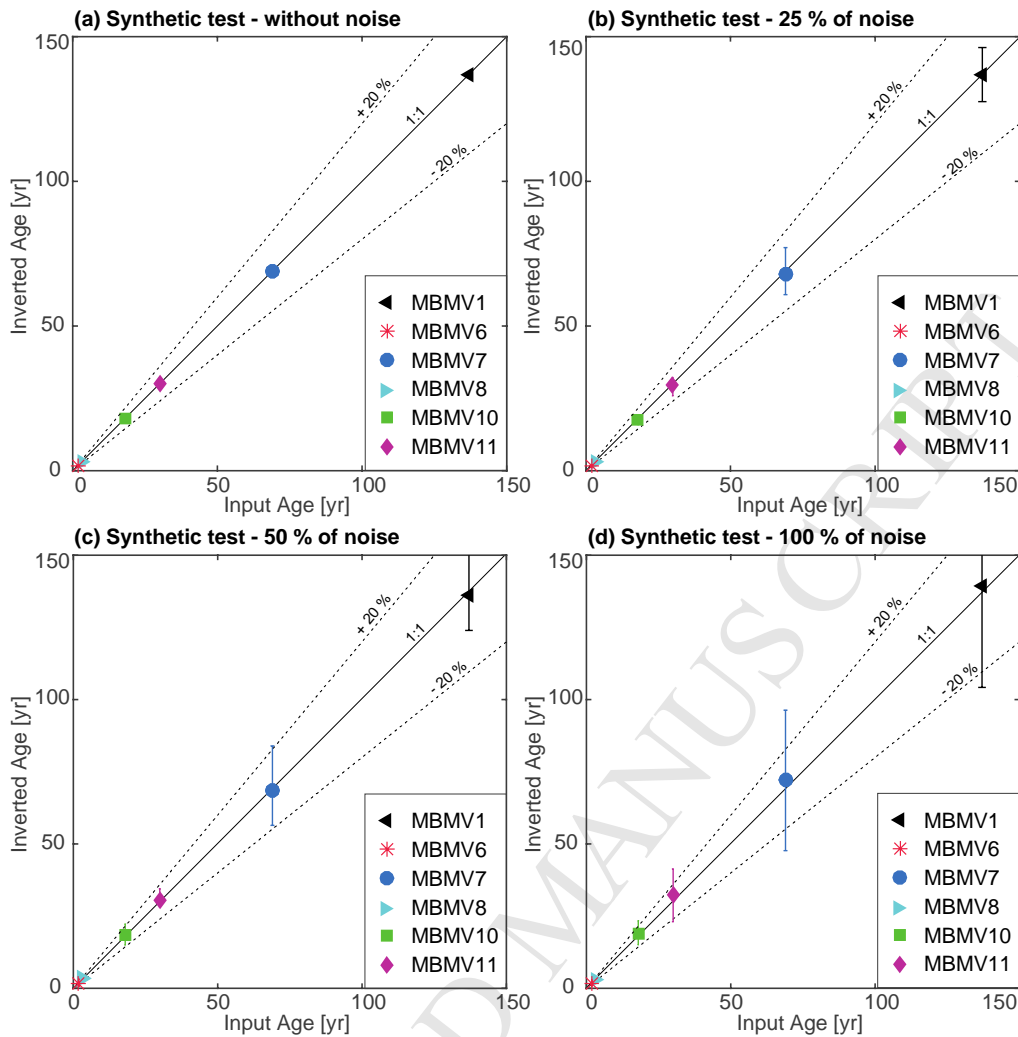
308
309 **Figure 5:** Results (median value) of inverted exposure age from the synthetic test, (a) without noise on
310 the luminescence signal, (b) with 25%, (c) 50%, and (d) 100% noise. Error bars represent $\pm 2\sigma$ on the
311 inverted age.

312 **4. Sample preparation and analysis**

313 The bedrock samples were cored to 30 mm depth using a Husqvarna DM220 drill, with 10-mm
314 diameter. Cores were then sliced into 0.7-mm thick rock slices with a BUEHLER IsoMet low speed
315 saw equipped with a 0.3-mm thick diamond blade. The samples were drilled and sliced under wet
316 conditions (water and lubricant, respectively) to avoid any heating that could potentially reset the OSL
317 signal. Sample preparation was done under subdued red light conditions. The thickness of each rock
318 slice was measured to determine the precise depth of each luminescence measurement.

319   All luminescence measurements were performed using Risø TL-DA 20 TL/OSL luminescence
320 readers (Bøtter-Jensen et al., 2010) equipped with ^{90}Sr beta sources at the University of Lausanne
321 (Switzerland). The readers have dose rates of ~0.1 and ~0.2 Gy s^{-1} and measurement reproducibility of
322 1.14 % and 1.26 % respectively. We first perform a preheat at 250 °C before giving infrared (IR)
323 stimulation (870 nm, FWHM 40 nm) at 50 °C. Luminescence signals are detected through a filter

12

324 combination of a Schott BG-3 and Schott BG-39. A uniform test dose was used (27.2 Gy) to measure

325 the subsequent luminescence response (T_x) and to normalize the natural infrared stimulated

326 luminescence (IRSL) signal (L_x) for every rock slice. Infrared stimulated luminescence was measured

327 for 200 s and signals were integrated over the first 6 seconds whereas the background signal was

328 integrated between 70-100 seconds. Measurements were analysed using Analyst v.3.22b (Duller,

329 2005). All thermal treatments and stimulations at temperatures greater than 200℃ (i.e. preheat step)

330 were carried out in nitrogen atmosphere. The experimental approach was validated using a dose

331 recovery and preheat plateau test (see Supplementary Material A3; Murray and Wintle, 2000; Wintle

332 and Murray, 2006).

333 **5. Results**

334 **5.1. Experimental results**

335 Figure 6 shows the luminescence measurements for representative samples MBMV1 and MBMV10

336 (results of the others samples are presented in Fig. 8). Three replicates (i.e. individual cores) per

337 sample were sliced in a way that a depth and an IRSL signal can be attributed to each rock slice

338 (unique colour/symbol for each individual rock slice in Fig. 6). The results show similar behaviour

339 between the different cores for a given sample (Fig. 6). The IRSL signal is bleached near the surface

340 and reaches a plateau at depth. Furthermore, and more importantly, the transition from a bleached

341 signal to the plateau varies with the exposure age. The three core measurements reproduce well for

342 both samples illustrated in Figure 6, with the mean standard deviation between the three cores ranging

343 from 7 to 27% for all the studied samples. These results confirm experimentally that cores extracted

344 from one individual sample record the same exposure history, supporting the proposed approach.

345
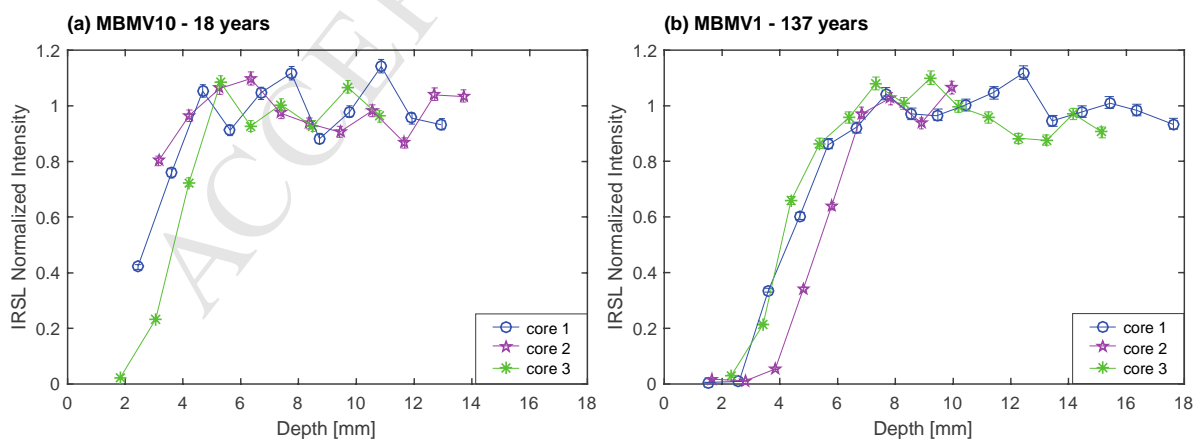
346

347 **Figure 6:** Infrared stimulated luminescence (IRSL) signal with depth for samples (a) MBMV10 and

348 (b) MBMV1. Each coloured data point represents an individual rock slice. IRSL signals were

349 normalized by L_0, which was determined by taking the average of the luminescence measurements

along the plateau. The plateau was defined when the luminescence signal is fluctuating by less than 20%.

5.2. Independent parameter determination

In this section, we determine the $\overline{\sigma\varphi}_0$ and μ parameters individually for each sample in order to study their potential variability from one rock surface to another (Table 3). As explained in Section 3.2, bedrock surfaces from the same location should share a common $\overline{\sigma\varphi}_0$ parameter (i.e. same order of magnitude; Blumthaler et al., 1997). Similarly, we expect that the μ parameter should be similar for samples from a uniform lithology. The determined parameters are then used in the inversion of the exposure ages for each sample individually (see Section 5.5). All inversion outcomes are summarized in Table 3. Samples MBMV1, MBMV8, MBMV10 and MBMV11 share similar effective decay rates ($\overline{\sigma\varphi}_0$) with the same order of magnitude (from $1.4\ 10^{-8}$ to $2.\ 10^{-7}\ s^{-1}$) and show attenuation coefficients (μ) between 1.07 and 1.89 mm^{-1}. Samples MBMV6 and MBMV7 behave differently with much lower effective decay rates ($\overline{\sigma\varphi}_0$ of $2.0\ 10^{-6}$ and $4.2\ 10^{-6}\ s^{-1}$, respectively), and different attenuation coefficients (μ of 0.92 and 2.50 mm^{-1}, respectively).

5.3. Parameter determination from joint probability estimates

We evaluate now the parameter determination from joint probability estimates in order to illustrate the benefit of having several known-age calibration samples. Figure 7a presents modelled results for sample MBMV10, which is representative of the other samples (except MBMV6 and MBMV7, see Section 5.2). The results show that $\log(\overline{\sigma\varphi}_0)$ and μ co-vary, which we attribute to measurement uncertainties and variability between the different cores. Figure 7b shows the area of acceptable fits when all the gneissic samples are included (i.e. excluding the granitic sample MBMV6).
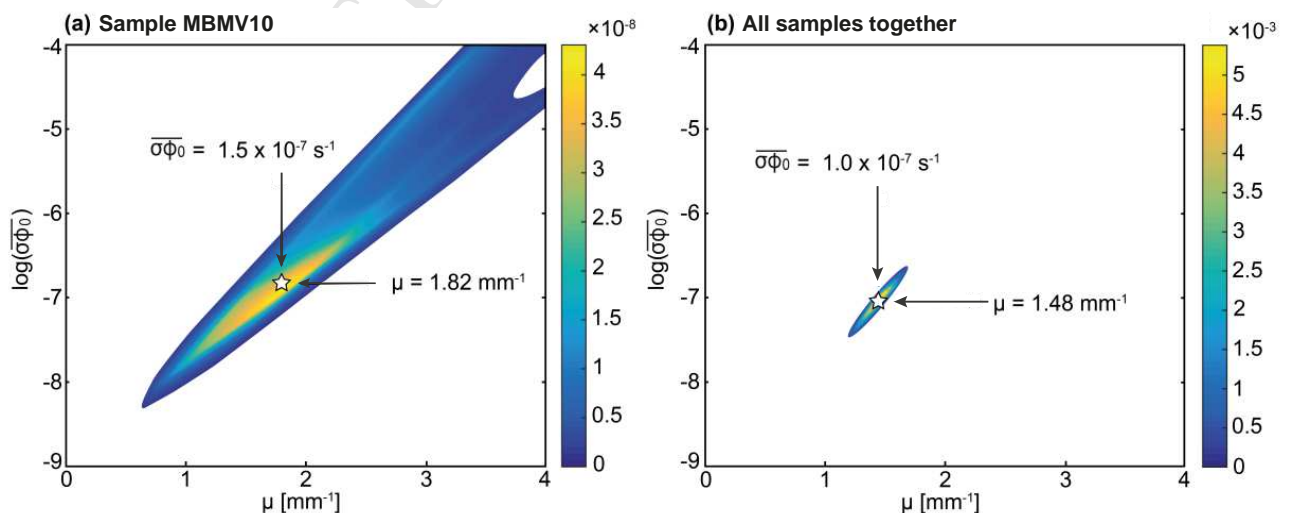
374 **Figure 7:** Relationship between the $\overline{\sigma\varphi}_0$ and μ parameters (a) for sample MBMV10, and (b) for all of
375 the gneiss samples (i.e. excluding MBMV6) enabling determination of the shared $\overline{\sigma\varphi}_0$ and μ
376 parameters ($1.0 \ 10^{-7}$ s^{-1} and 1.48 mm^{-1} respectively). For both figures, the colour scale shows the
377 likelihood between modelled and experimental data (Eq. 6, note the differences in scaling between the
378 two panels), and the star is the best-fit parameter values. Zero probability is not shown for clarity.

379

380 We then contrasted individual estimates of $\overline{\sigma\varphi}_0$ and μ for each sample, using different
381 combinations of samples to estimate these parameters. The results are summarized in Tables 3 and A3.
382 When inverting the model parameters with any combinations of three samples, all estimates of the
383 effective decay rates are between $6.6 \ 10^{-8}$ and $1.4 \ 10^{-7}$ s^{-1}, and all estimates of the attenuation
384 coefficients are between 1.33 and 1.57 mm^{-1}. Combinations of four samples provide $\overline{\sigma\varphi}_0$ values
385 ranging from $7.2 \ 10^{-8}$ to $1.2 \ 10^{-7}$ s^{-1} and μ values between 1.38 and 1.53 mm^{-1}. According to Table 3
386 and Figure 7b, a common likelihood exists for all the gneissic samples calibrated together, giving an
387 effective decay rate of $1.0 \ 10^{-7}$ s^{-1} and an attenuation coefficient of 1.47 mm^{-1}.

388 Figure 8 depicts the normalized IRSL signals measured for all samples and their individually-
389 constrained best-fit models (red lines) as described previously and illustrated in Figure 7a. The
390 obtained outcomes show that the proposed model accurately describes the luminescence bleaching
391 process through depth and time. The best-fit model calibrated with all of the gneissic samples together
392 (black dashed lines, parameters in Table 3) fits close to the best-fit model determined for each sample
393 individually (except MBMV6). These results confirm a key objective of the study, which is the
394 possibility to calibrate the model parameters using different surfaces along a vertical profile, with the
395 same lithology and different (independently-determined) exposure ages.

396

397 **Table 3:** Best-fit values of $\overline{\sigma\varphi}_0$ and μ determined for every sample individually and for all samples
398 excluding MBMV6. Combinations of three or four samples are presented in Table A3 (Supplementary
399 Material).

400

Parameter	$\overline{\sigma\varphi}_0$ [s^{-1}]			μ [mm^{-1}]		
Samples	Best-fit	+1σ	-1σ	Best-fit	+1σ	-1σ
Individually						
MBMV1	$1.4 \ 10^{-8}$	$1.5 \ 10^{-8}$	$1.3 \ 10^{-8}$	1.07	1.08	1.05
MBMV6	$2.0 \ 10^{-6}$	$2.2 \ 10^{-6}$	$1.8 \ 10^{-6}$	0.92	0.95	0.92
MBMV7	$4.0 \ 10^{-6}$	$5.0 \ 10^{-6}$	$3.6 \ 10^{-6}$	2.52	2.56	2.46
MBMV8	$2.2 \ 10^{-7}$	$2.4 \ 10^{-7}$	$1.5 \ 10^{-7}$	1.89	1.98	1.70
MBMV10	$1.5 \ 10^{-7}$	$1.5 \ 10^{-7}$	$1.1 \ 10^{-7}$	1.82	1.87	1.75
MBMV11	$4.2 \ 10^{-8}$	$5.3 \ 10^{-8}$	$3.9 \ 10^{-8}$	1.21	1.22	1.13
All samples together excluding MBMV6	$1.0 \ 10^{-7}$	$1.1 \ 10^{-7}$	$9.5 \ 10^{-8}$	1.48	1.50	1.44

401

402
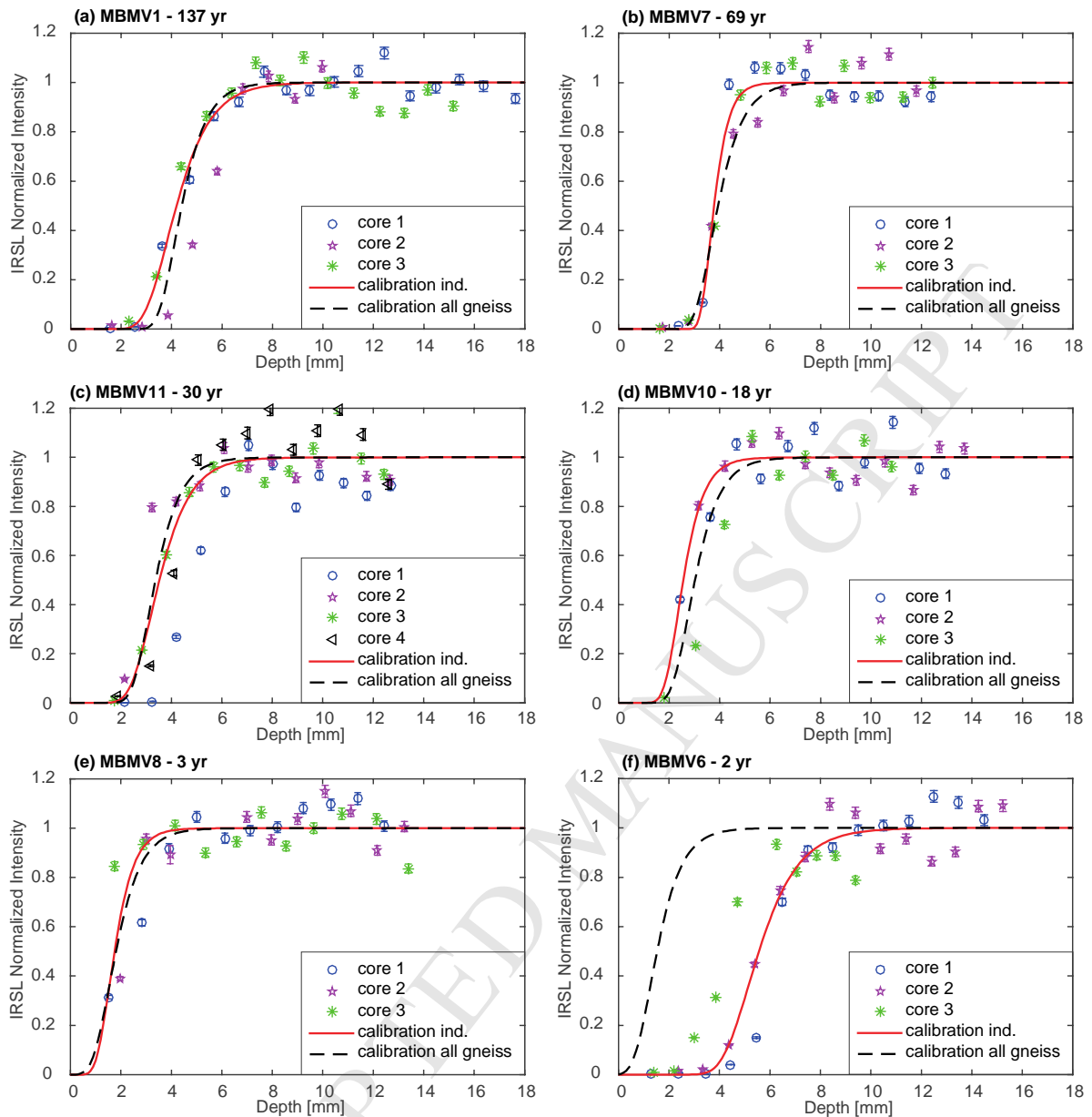
Figure 8: Normalized infrared stimulated luminescence (IRSL) profiles with depth and best-fit models. Coloured data point represents individual rock slice (each symbol/colour represents one core). The red lines show the best-fit model for each sample taken individually. The dashed black lines represent the best-fit model from a common calibration of the parameters using all gneiss samples together ($\overline{\sigma\varphi}_0 = 1.0 \ 10^{-7}$ s^{-1} and $\mu = 1.48$ mm^{-1}, cf. Fig. 7b and Table 3). Raw IRSL data are presented in Table A3(Supplementary Material).

5.4. Evolution of the luminescence signal through time

Compiling the best-fit models determined for each sample individually, a positive correlation between the exposure age and the depth at which the natural IRSL signal is zeroed can be clearly observed for samples within the same lithology (Fig. 9a). If we consider the inflection point of each individual model ($Lx/Tx = 0.5$ on Fig. 9a) as a proxy for the bleaching depth, this value ranges between 1.7 and

414   4.2 mm for 3 and 137 years of daylight exposure, respectively (Fig. 9b). The granitic sample MBMV6

415   does not follow this correlation, its bleaching depth being at 7 mm after 2-yr exposure to daylight.

416

417
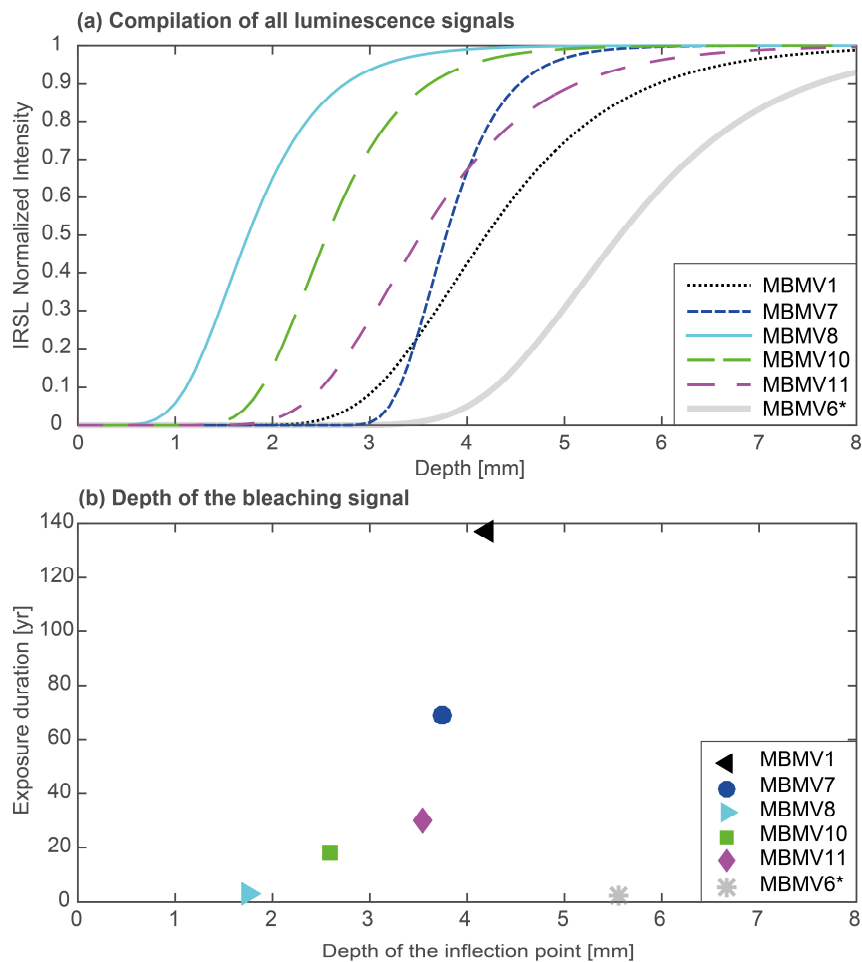
418   **Figure 9:** (a) Compilation of the best-fit models for each individual sample (cf. red lines in Fig. 8). (b)

419   Correlation between the IRSL bleaching depth (i.e. the inflection point of the models presented in (a))

420   and the exposure age of each individual sample. The * symbol indicates the granitic sample

421   (MBMV6); all the other samples are gneiss.

422   **5.5. Inversion for exposure age**

423   Once the model parameters have been determined by different sample combinations, it is possible to

424   subsequently invert the exposure age as explained above. Figure 10 compares the exposure ages

425   inverted from the different sample combinations, with the observed exposure age (all results are

426   compiled in the Supplementary Table A4 and Figure A3). Figure 10a shows that our modelling

427   approach is able to recover the observed exposure ages using parameters determined for each

428   individual sample (<10% difference). When the exposure ages are inverted using the parameters

429   determined for all of the gneissic samples together (as shown in Fig. 7b), there are slight differences

430   between the inverted exposure age and independent age control (Fig. 10b, Table A4 and Figure A3).

431 The inverted ages are almost all within 20% of the observed ages except for sample MBMV11, which
432 is overestimated by 90%.

433   Taking different calibration combinations with four (Fig. 10c) or three (Fig. 10d) samples also
434 results in different performance regarding age predictions. For all gneissic samples, except MBMV11,
435 the inverted exposure ages at 2σ are still within 20% of the observed ages. Note that in our approach
436 the inverted exposure ages with four and three samples calibrations are only shown when the specific
437 sample is not part of the calibration combination (grey shadow in the Supplementary Table A4).
438 Although the match between the inverted and observed ages, as well as the trend between samples, is
439 preserved independent of the calibration approach, our results show that the higher the number of
440 calibration sites is, the better the inversion of exposure ages would be.

441
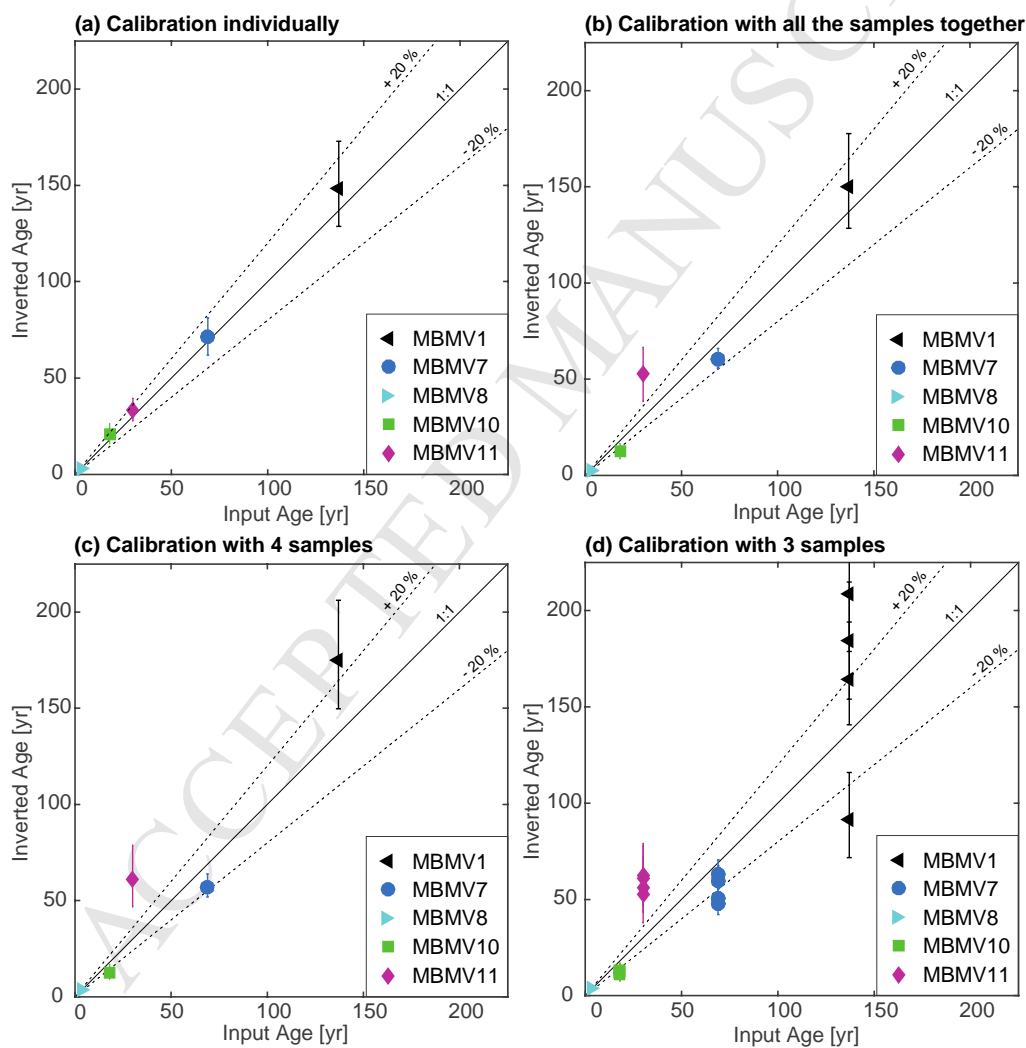
443 **Figure 10:** Correlation between inverted (median values) and observed exposure ages resulting from
444 different calibration combinations to constrain the model parameters. The error bars on the inverted
445 exposure ages are ±2σ as presented in Table 3 (all results presented in the Supplementary Table A4).

18

446 **6**. **Discussion**

447 Our results from the Mer de Glace glacier have allowed to validate, over post-LIA timescales (i.e. over

448 2-137 years), the assumption that the longer a rock surface has been exposed to daylight, the deeper

449 the luminescence signal has been bleached (Polikreti et al., 2002; 2003; Sohbati et al., 2011; 2012).

450 Using the mathematical model propose by Sohbati et al. (2011), we accurately describe the time

451 evolution of luminescence within a rock column. The different combinations of samples used to

452 calibrate the model give parameter values ($\overline{\sigma\varphi}_0$ and μ) that are on the same order of magnitude for

453 samples within similar regions and lithology, and which agree with literature values (Sohbati et al.,

454 2011; 2012a,b).

455 　　　　We also observe that the evolution of luminescence signals with both time and depth within

456 bedrock is mainly controlled by rock characteristics (lithology, texture, weathering and mineral

457 composition). These rock properties will govern the light attenuation and penetration into rocks

458 (parameter μ in Eq. 4), and thus the net bleaching effect on the luminescence signal. At the regional

459 scale, the lithology should preferably be uniform to enable model calibration on some known-age

460 surfaces (through independent dating) before application to reconstruct the exposure history of other

461 bedrock surfaces with unknown exposure age. We see that in a granitic rock, comprising coarse quartz

462 and feldspar grains (translucent minerals), the luminescence-bleaching front will propagate much

463 faster than in gneiss bedrock.

464 　　　　Our inversion approach to constrain rock surface exposure ages from OSL data, reveals that

465 the number of calibration samples is critical for constraining the model parameters and thus obtaining

466 accurate exposure ages. Fortunately, calibration rock surfaces in periglacial environments can often be

467 found from historical or remote-sensing paleo-glacier reconstructions. Other types of bedrock surfaces

468 can be used for independent constraint, e.g. anthropogenic structures such as road-cut outcrops (e.g.

469 Sohbati et al., 2012a) or landslide scars. The combined investigation of OSL systems with other

470 surface exposure dating methods such as terrestrial *in situ* cosmogenic nuclides will also enable us to

471 quantitatively assess the method's accuracy over longer timescales such as the late Pleistocene.

472 　　　　Experimental luminescence data presented in Figure 8 confirms that each individual sample's

473 exposure history has been recorded in its luminescence depth profile. For the six bedrock surfaces

474 studied here, each luminescence profile exhibits a fully-bleached signal at shallow depth (i.e. from 1 to

475 7 mm depending on both the exposure age and lithology, Fig. 9), followed by a sharp transition to a

476 plateau of intensity deeper into the rock. These simple and homogeneous luminescence profiles can be

477 compared with complex profiles previously observed following multi-stage exposure histories

478 obtained from buried cobbles (Freiesleben et al., 2015; Sohbati et al., 2015). This confirms that the

479 glacially-polished surfaces we sampled along the Montenvers cross-sections have experienced a

480 simple exposure history. Furthermore, field evidence for surface preservation with glacial features

481 (striations, flutes) indicate that the bedrock surfaces have been eroded and polished by subglacial

482 processes before deglaciation. Weathering or mechanical erosion may lead to an underestimation of

483 the true exposure age. Thereby, the inferred exposure history from these well-preserved rock surfaces

484 can be used to reconstruct the paleo-glacier thickness and extent since the LIA.

485 Bleaching of the OSL signal has occurred at less than 1 cm depth below the exposed surface

486 after more than 137 years of daylight exposure, highlighting the high temporal resolution of this novel

487 method for paleo-glacier reconstruction. In mountainous locations such as the Mont Blanc massif,

488 where the glacial history has been complex with several glacier fluctuations during the late Pleistocene

489 to Holocene (recurrent retreat/advance cycles; e.g. LeRoy et al., 2015), the application of absolute

490 dating methods such as terrestrial *in situ* cosmogenic nuclides are difficult due to potential inheritance

491 from previous exposure events (e.g. Goehring et al., 2011). One of the main advantages of OSL

492 surface exposure dating is that daylight bleaching of the OSL signal occurs within the first few

493 millimetres below the exposed rock surface. Short glacier re-advances over the late Holocene (e.g.

494 LeRoy et al., 2015) would have easily eroded the first centimetres of bedrock, consequently resetting

495 the OSL system before the post-LIA glacier retreat. We have thus shown in this study that well-

496 preserved polished bedrock surfaces can be used for the application of OSL surface exposure dating in

497 order to constrain the timing of the last glacial retreat from the LIA to present day, improving our

498 temporal resolution for glacier reconstruction. Over such timescales, the contribution of the trap filling

499 rate ($F(x)$ in Section 2.3) from radioactive decay in gneissic or granitic rock can be assumed to be

500 negligible (see Supplementary material A2). However, this contribution may have to be taken into

501 account when extending paleo-glacier reconstruction using OSL surface exposure dating to longer

502 timescales, e.g. since the Last Glacial Maximum or further back into the Quaternary. Over the same

503 timescales, weathering and erosion of the surface are likely to play a significant role.

504 **7. Conclusions**

505 In this study, we have investigated the potential of OSL surface exposure dating for quantitatively

506 reconstructing post-LIA glacier retreat. We worked along an altitudinal cross-section of the Mer de

507 Glace glacier (Mont Blanc massif, France), and collected glacially-polished bedrock surfaces with

508 known exposure ages (from 3 to 137 years) along the Montenvers profile from around 1841 m.a.s.l.

509 elevation to the present-day glacier position (1696 m.a.s.l.). We have developed a statistical approach

510 to calibrate the bleaching model parameters from known-age samples. Experimental IRSL depth-

511 profile data for five different polished bedrock surfaces show an increase of the luminescence signal

512 bleaching depth with exposure age. We conclude that OSL surface exposure dating can be applied to

513 glacial and periglacial environments, and is a promising tool for high-resolution reconstruction of

514 recent ice-extent and thickness fluctuations, both in space and time. However, we find that several

515 calibration samples must be used to calibrate the model parameters before inferring exposure ages on

516 bedrock surfaces within a specific area, taking into account the potential variation in bedrock

517 lithology. We also find that measurement uncertainties, intrinsic data noise or both can result in large

518 uncertainties on inverted ages, especially when applying this method over 10^3-10^4 yr timescales.

527 **References**

528 Aitken, M.J., 1985. Thermoluminescence dating. Academic press.

529 Aitken, M.J., 1998. An Introduction to Optical Dating The Dating of Quaternary: Sediments by the

530   Use of Photon-stimulated Luminescence. Oxford University press.

531 Bailey, R.M., 2004. Paper I-simulation of dose absorption in quartz over geological timescales and its

532   implications for the precision and accuracy of optical dating. Radiation Measurements 38, 299-310.

533 Baillie M.G.L., 1995. A Slice Through Time: dendrochronology and precision dating. London,

534   Routledge, 176 p.

535 Balco, G., 2011. Contributions and unrealized potential contributions of cosmogenic nuclide exposure

536   dating to glacier chronology, 1990-2010. Quaternary Science Reviews 30, 3-27.

537 Bini, A., Buoncristiani, J.F., Couterrand, S., Ellwanger, D., Felber, M., Florineth, D., Graf, H.R.,

538   Keller, O., Kelly, M., Schlüchter, C., Schoeneich, P., 2009. Switzerland during the Last Glacial

539   Maximum 1: 500,000. Bundesamt für Landestopografie swisstopo.

540 Blumthaler, M., Ambach, W., Ellinger, R., 1997. Increase in solar UV radiation with altitude. Journal

541   of Photochemistry and Photobiology B: Biology 39, 130-134.

542 Bøtter-Jensen, L., Thomsen, K.J., Jain, M., 2010. Review of optically stimulated luminescence (OSL)

543   instrumental developments for retrospective dosimetry. Radiation Measurements 45, 253-257.

544 Broecker, W., Denton, G., 1990. What drives glacial cycles? Scientific American 262, 43-50.

545 Brown, N.D., Rhodes, E.J., Harrison, T.M., 2017. Using thermoluminescence signals from feldspars

546   for low-temperature thermochronology. Quaternary Geochronology 42, 31-41.

547 Coutterand, S., Buoncristiani, J.-F., 2006. Paléogéographie du dernier maximum glaciaire du

548   Pléistocène récent de la région du massif du Mont Blanc, France. Quaternaire. Revue de

549   l'Association française pour l'étude du Quaternaire 17, 35-43.

550 Dobmeier, C., 1998. Variscan P–T deformation paths from the southwestern Aiguilles Rouges massif
551   (External massif, western Alps) and their implication for its tectonic evolution. Geologische
552   Rundschau 87, 107-123.

553 Duller GAT. 2005. Luminescence Analyst. University of Wales: Aberystwyth.

554 Duller, G.A.T., 2008. Single-grain optical dating of Quaternary sediments: why aliquot size matters in
555   luminescence dating. Boreas 37, 589-612.

556 Egholm, D., Nielsen, S., Pedersen, V.K., Lesemann, J.-E., 2009. Glacial effects limiting mountain
557   height. Nature 460, 884-887.

558 Ehlers, J., Gibbard, P.L., 2007. The extent and chronology of Cenozoic Gobal Glaciation. Quaternary
559   International 164-165, 6-20.

560 Freiesleben, T., Sohbati, R., Murray, A., Jain, M., Al Khasawneh, S., Hvidt, S., Jakobsen, B., 2015.
561   Mathematical model quantifies multiple daylight exposure and burial events for rock surfaces using
562   luminescence dating. Radiation Measurements 81, 16-22.

563 Fuchs, M., Owen, L.A., 2008. Luminescence dating of glacial and associated sediments: review,
564   recommendations and future directions. Boreas 37, 636-659.

565 Gardent, M., Rabatel, A., Dedieu, J.-P., Deline, P., 2014. Multitemporal glacier inventory of the
566   French Alps from the late 1960s to the late 2000s. Global and Planetary Change 120, 24-37.

567 Goehring, B.M., Schaefer, J.M., Schluechter, C., Lifton, N.A., Finkel, R.C., Jull, A.T., Akçar, N.,
568   Alley, R.B., 2011. The Rhone Glacier was smaller than today for most of the Holocene. Geology
569   39, 679-682.

570 Goehring, B.M., Vacco, D.A., Alley, R.B., Schaefer, J.M., 2012. Holocene dynamics of the Rhone
571   Glacier, Switzerland, deduced from ice flow models and cosmogenic nuclides. Earth and Planetary
572   Science Letters 351, 27-35.

573 Guralnik, B., Jain, M., Herman, F., Ankjærgaard, C., Murray, A.S., Valla, P.G., Preusser, F., King,
574   G.E., Chen, R., Lowick, S.E., 2015. OSL-thermochronometry of feldspar from the KTB borehole,
575   Germany. Earth and planetary science letters 423, 232-243.

576 Habermann, J., Schilles, T., Kalchgruber, R., Wagner, G.A., 2000. Steps towards surface dating using
577   luminescence. Radiation Measurements 32, 847-851.

578 Hajdas, I., 2008. Radiocarbon dating and its applications in Quaternary studies. Eiszeitalter und
579   Gegenwart Quaternary Science Journal 57, 24.

580 Herbert, T.D., Lawrence, K.T., Tzanova, A., Peterson, L.C., Caballero-Gill, R., Kelly, C.S., 2016.
581   Late Miocene global cooling and the rise of modern ecosystems. Nature Geosci 9, 843-847.

582 Hippe, K., Ivy-Ochs, S., Kober, F., Zasadni, J., Wieler, R., Wacker, L., Kubik, P.W., Schlüchter, C.,
583   2014. Chronology of Lateglacial ice flow reorganization and deglaciation in the Gotthard Pass area,
584   Central Swiss Alps, based on cosmogenic [10]Be and in situ [14]C. Quaternary Geochronology 19, 14-
585   26.

586   Huntley, D.J., Godfrey-Smith, D.I., Thewalt, M.L., 1985. Optical dating of sediments. Nature 313,
587   105-107.

588   Ivy-Ochs, S., 2015. Glacier variations in the European Alps at the end of the last glaciation. Cuadernos
589   de investigación geográfica 41, 295-315.

590   Ivy-Ochs, S., Kerschner, H., Reuther, A., Maisch, M., Sailer, R., Schaefer, J., Kubik, P.W., Synal, H.-
591   A., Schlüchter, C., 2006. The timing of glacier advances in the northern European Alps based on
592   surface exposure dating with cosmogenic 10Be, 26Al, 36Cl, and 21Ne. Geological Society of
593   America Special Papers 415, 43-60.

594   Ivy-Ochs, S., Kerschner, H., Maisch, M., Christl, M., Kubik, P.W., Schlüchter, C., 2009. Latest
595   Pleistocene and Holocene glacier variations in the European Alps. Quaternary Science Reviews 28,
596   2137-2149.

597   Ivy-Ochs, S., Briner, J.P., 2014. Dating disappearing ice with cosmogenic nuclides. Elements 10, 351-
598   356.

599   King, G., Herman, F., Lambert, R., Valla, P., Guralnik, B., 2016. Multi-OSL-thermochronometry of
600   feldspar. Quaternary Geochronology 33, 76-87.

601   Lal, D., 1991. Cosmic ray labeling of erosion surfaces: in situ nuclide production rates and erosion
602   models. Earth and Planetary Science Letters 104, 424-439.

603   Lang, A., Hönscheidt, S., 1999. Age and source of colluvial sediments at Vaihingen-Enz, Germany.
604   Catena 38, 89-107.

605   Laskaris, N., Liritzis, I., 2011. A new mathematical approximation of sunlight attenuation in rocks for
606   surface luminescence dating. Journal of Luminescence 131, 1874-1884.

607   Le Roy, M., Nicolussi, K., Deline, P., Astrade, L., Edouard, J.-L., Miramont, C., Arnaud, F., 2015.
608   Calendar-dated glacier variations in the western European Alps during the Neoglacial: the Mer de
609   Glace record, Mont Blanc massif. Quaternary Science Reviews 108, 1-22.

610   Lean, J., 1987. Solar Ultraviolet Irradiance Variations: A review. Journal of Geophysical Research
611   92,839-968.

612   Liritzis, I., 1994. A new dating method by thermoluminescence of carved megalithic stone building.
613   Comptes rendus de l'Académie des sciences. Série 2. Sciences de la terre et des planètes 319, 603-
614   610.

615   Liritzis, I., 2011. Surface dating by luminescence: an overview. Geochronometria 38, 292-302.

616   Molnar, P., England, P., 1990. Late Cenozoic uplift of mountain ranges and global climate change:
617   chicken or egg? Nature 346, 29-34.

618   Murray, A.S., Wintle, A.G., 2000. Luminescence dating of quartz using an improved single-aliquot
619   regenerative-dose protocol. Radiation measurements 32, 57-73.

620   Nussbaumer, S., Zumbühl, H.J., Steiner, D., 2007. Fluctuations of the Mer de glace (Mont Blanc area,
621   France) AD 1500-2050. An interdisciplinary approach using new historical data and neural
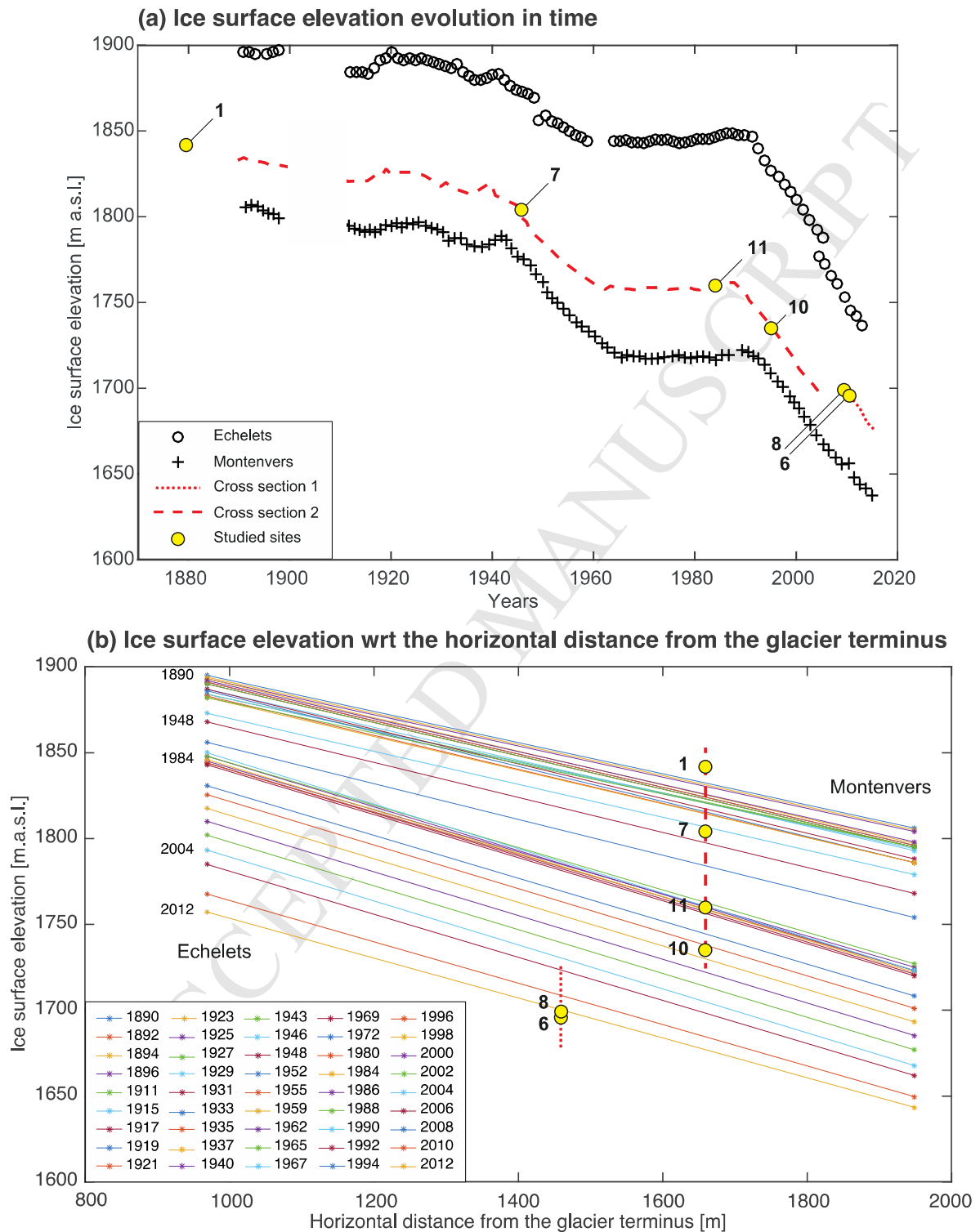622   network simulations. Zeitschrift für Gletscherkunde und Glazialgeologie ZGG, 5-175.

623 Peizhen, Z., Molnar, P., Downs, W.R., 2001. Increased sedimentation rates and grain sizes 2–4 Myr
624   ago due to the influence of climate change on erosion rates. Nature 410, 891-897.

625 Penck, A., 1905. Glacial features in the surface of the Alps. The Journal of Geology 13, 1-19.

626 Preusser, F., Graf, H.R., Keller, O., Krayss, E., Schlüchter, C., 2011. Quaternary glaciation history of
627   northern Switzerland. Quaternary Science Journal 60(2-3), 282-305.

628 Polikreti, K., Michael, C., Maniatis, Y., 2002. Authenticating marble sculpture with
629   thermoluminescence. Ancient TL 20, 11-18.

630 Polikreti, K., Michael, C., Maniatis, Y., 2003. Thermoluminescence characteristics of marble and
631   dating of freshly excavated marble objects. Radiation Measurements 37, 87-94.

632 Rabatel, A., Letréguilly, A., Dedieu, J., Eckert, N., 2013. Changes in glacier equilibrium-line altitude
633   in the western Alps from 1984 to 2010: evaluation by remote sensing and modeling of the morpho-
634   topographic and climate controls. Cryosphere 7, p. 1455-p. 1471.

635 Rhodes, E.J., 2011. Optically stimulated luminescence dating of sediments over the past 200,000
636   years. Annual Review of Earth and Planetary Sciences 39, 461-488.

637 Richards, M.P., 1994. Luminescence dating of quartzite from the Diring Yuriakh site. M.A. Thesis,
638   Simon Fraser University, unpublished.

639 Schimmelpfennig, I., Schaefer, J.M., Akçar, N., Koffman, T., Ivy-Ochs, S., Schwartz, R., Finkel, R.C.,
640   Zimmerman, S., Schlüchter, C., 2014. A chronology of Holocene and Little Ice Age glacier
641   culminations of the Steingletscher, Central Alps, Switzerland, based on high-sensitivity beryllium-
642   10 moraine dating. Earth and Planetary Science Letters 393, 220-230.

643 Simms, A.R., DeWitt, R., Kouremenos, P., Drewry, A.M., 2011. A new approach to reconstructing sea
644   levels in Antarctica using optically stimulated luminescence of cobble surfaces. Quaternary
645   Geochronology 6, 50-60.

646 Simkins, L.M., Simms, A.R., DeWitt, R., 2013. Relative sea-level history of Marguerite Bay,
647   Antarctic Peninsula derived from optically stimulated luminescence-dated beach cobbles.
648   Quaternary Science Reviews 77, 141-155.

649 Singarayer, J.S., 2002. Linearly modulated optically stimulated luminescence of sedimentary quartz:
650   Physical mechanisms and implications for dating. D.Phil. thesis, University of Oxford. 345 pp.

651 Sohbati, R., Murray, A., Jain, M., Buylaert, J.-P., Thomsen, K., 2011. Investigating the resetting of
652   OSL signals in rock surfaces. Geochronometria 38, 249-258.

653 Sohbati, R., Jain, M., Murray, A., 2012a. Surface exposure dating of non-terrestrial bodies using
654   optically stimulated luminescence: A new method. Icarus 221, 160-166.

655 Sohbati, R., Murray, A.S., Buylaert, J.-P., Almeida, N.A.C., Cunha, P.P., 2012b. Optically stimulated
656   luminescence (OSL) dating of quartzite cobbles from the Tapada do Montinho archaeological site
657   (east-central Portugal). Boreas 41, 452-462.

658 Sohbati, R., Murray, A., Porat, N., Jain, M., Avner, U., 2015. Age of a prehistoric "Rodedian" cult site
659   constrained by sediment and rock surface luminescence dating techniques. Quaternary
660   Geochronology 30, 90-99.

661 Theocaris, P., Liritzis, I., Galloway, R., 1997. Dating of two Hellenic pyramids by a novel application
662   of thermoluminescence. Journal of Archaeological Science 24, 399-405.

663 Vafiadou, A., Murray, A., Liritzis, I., 2007. Optically stimulated luminescence (OSL) dating
664   investigations of rock and underlying soil from three case studies. Journal of Archaeological
665   Science 34, 1659-1669.

666 Valla, P.G., Lowick, S.E., Herman, F., Champagnac, J.-D., Steer, P., Guralnik, B., 2016. Exploring
667     $IRSL_{50}$ fading variability in bedrock feldspars and implications for OSL thermochronometry.
668   Quaternary Geochronology 36, 55-66.

669 Vincent, C., Harter, M., Gilbert, A., Berthier, E., Six, D., 2014. Future fluctuations of Mer de Glace,
670   French Alps, assessed using a parameterized model calibrated with past thickness changes. Annals
671   of Glaciology 55, 15-24.

672 Wirsig, C., Zasadni, J., Ivy-Ochs, S., Christl, M., Kober, F., Schlüchter, C., 2016. A deglaciation
673   model of the Oberhasli, Switzerland. Journal of Quaternary Science 31, 46-59.

674 Wintle, A.G., Murray, A.S., 2006. A review of quartz optically stimulated luminescence
675   characteristics and their relevance in single-aliquot regeneration dating protocols. Radiation
676   Measurements 41, 369-391.

677 Zachos, J.C., Shackleton, N.J., Revenaugh, J.S., Pälike, H., Flower, B.P., 2001. Climate response to
678   orbital forcing across the Oligocene-Miocene boundary. Science 292, 274-278.

679

680   **Supplementary Material**

681

682   **A1. Ice surface reconstruction**

(a) Ice surface elevation evolution in time

(b) Ice surface elevation wrt the horizontal distance from the glacier terminus

683

684   **Figure A1:** (a) Reconstruction of averaged ice-surface elevation [m.a.s.l.] through time along the Mer

685   de Glace glacier (see locations of cross-sections on Fig.1). Averaged ice-surface elevations at the

686   Montenvers (crosses) and Echelets (circles) cross-sections. The cross-sections 1 and 2 (red dashed

687 lines) have been interpolated from the Montenvers and Echelets cross-sections, and used to project the

688 studied samples (yellow circles). (b) Ice-surface elevation with respect to the horizontal distance from

689 the glacier terminus used for the interpolation of the Montenvers and Echelets cross-sections. The ice

690 surface elevations have been reconstructed from historical maps, survey reports and aerial

691 photogrammetry (modified from Vincent et al., 2014). The dataset was kindly provided by the French

692 glacier observatory GLACIOCLIM (http://www-lgge.ujf-grenoble.fr/ServiceObs/index.htm).

693

694 **A2. Dose rate sensitivity**

695 The sensitivity of luminescence signal evolution to the dose rate is tested after four different daylight

696 exposure times (1, 10, 100 and 1000 years of exposure), with a null dose rate and an extremely high

697 dose rate ($\dot{D} \approx 14$ Gy ka^{-1}, King et al., 2016). We used an equation developed by Sohbati et al. (2012)

698 describing the luminescence evolution $L(x)$ as a function of the exposure time t [s], depth x [mm],

699 charge detrapping rate $\overline{\sigma\varphi}_0$ [s^{-1}], attenuation factor μ [mm^{-1}], a sample-dependent constant that

700 characterises filling rate D_0 [Gy] and the natural dose rate $\dot{D}$ [Gy s^{-1}].

$$L(x) = \frac{\overline{\sigma\varphi}_0\, e^{-\mu x} e^{-t\left[\overline{\sigma\varphi}_0\, e^{-\mu x} + \frac{\dot{D}(x)}{D_0}\right]} + \frac{\dot{D}(x)}{D_0}}{\overline{\sigma\varphi}_0\, e^{-\mu x} + \frac{\dot{D}(x)}{D_0}} \tag{A1}$$

701

702

703 The resulting comparison shows that the luminescence signal is not sensitive to dose rate over

704 millenial timescales. We thus consider the dose rate as negligible for our applications of OSL surface

705 exposure dating, and do not take it into account in the luminescence evolution equation.

706
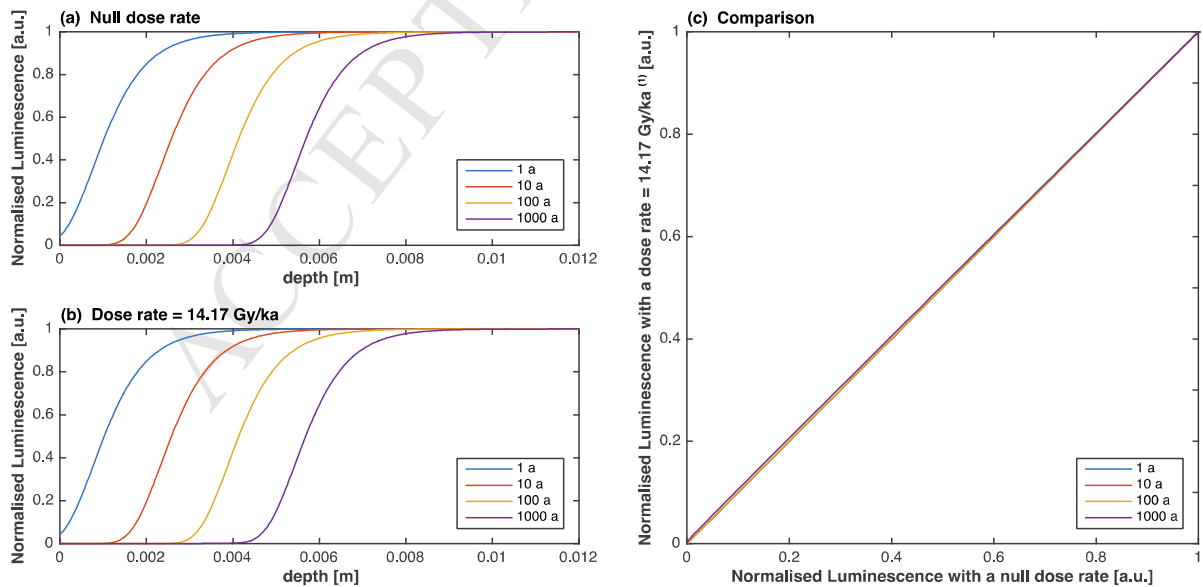
707

708 **Figure A2**: Evolution of the nomalised luminescence signal through time and depth for 1, 10, 100 and

709 1000 years of daylight exposure, taking into account (a) a null dose rate and (b) an extremely high

710   dose rate of ~14 Gy/ka (King et al., 2016). Inset (c) shows the comparison between the result with two

711   different dose rates.

712

713   **A3. Luminescence measurement tests**

714   The purpose of the following tests is to find the most appropriate infrared stimulated luminescence

715   (IRSL) measurement conditions for analysis of the collected samples from the Montenvers site. We

716   first performed a residual dose determination. Under natural daylight conditions, luminescence signals

717   of feldspar may not be completely reset, leaving a residual dose. The residual test allows the

718   evaluation of this remaining natural dose (which may also originate from other sources e.g. thermal

719   transfer). We first reset the luminescence signal by exposing rock slices (3 slices for a representative

720   sample of Montenvers site) to daylight for about 3 hours before analysing both slide sides. We then

721   measured the residual dose using infrared stimulation at 50°C (IRSL$_{50}$) following different preheat

722   temperatures (during 60 s). The residual dose after a preheat temperature of 250°C is 0.25 ± 0.45 Gy.

723   With preheat temperature equal to 275°C, the residual dose is 0.85 ± 0.43 Gy. For preheat temperature

724   equal to 300°C and 325°C, the residual doses increase to 2.94 ± 0.41 Gy and 2.10 ± 0.52 Gy

725   respectively.

726   We then proceeded to a dose recovery test with preheat-plateau to determine the most

727   appropriate preheat temperature. Thereby we quantified the recovered doses with IRSL$_{50}$ for the same

728   range of preheat temperatures explored in the residuals test. We analyzed 3 rock slices with a

729   laboratory beta dose of 27.25 Gy after complete optical bleaching (both disk sides exposed to daylight

730   for about 3 hours). The samples were not heated prior the daylight bleaching. Preheat temperatures

731   250°C, 275°C, 300°C, 325°C were investigated, and results are corrected for the residual dose values

732   reported in Table A1. For preheat temperatures of 250°C, 275°, 300°C and 325°C, we obtained dose

733   recovery ratios of 0.90 ± 0.10, 0.87 ± 0.17, 0.77 ± 0.23 and 0.85 ± 0.15, respectively (Table A1). The

734   optimal preheat temperature for both the residual dose and dose recovery is thus 250°C, and was used

735   in all subsequent experiments.

736   **Table A1:** Results of the residual test and the dose recovery preheat plateau test after a given beta
737   dose of 27.25 Gy.
738

Preheat Temperature (°C)	250	275	300	325
Residual dose (Gy)	0.25 ± 0.45	0.85 ± 0.43	2.94 ± 0.41	2.1 ± 0.52
Dose recovery ratio	0.9 ± 0.10	0.87 ± 0.17	0.77 ± 0.23	0.85 ± 0.15

739
740
741   **Table A2:** Sensitivity corrected luminescence signal intensities with depth. The depth x (cm) is

742   measured during core slicing with a high-precision numerical micrometre. IRSL measurements

28

743 (*Lx/Tx)* are the results of the luminescence analysis (as explained in Section 4) and the analytical error

744 on the measurement (*Lx/Tx err.)* is calculated in Analyst v.4.31.7 including a measurement error of

745 1.5%. Note: Each line corresponds to the measurement of one single rock slice.

	MBMV1			MBMV6			MBMV7			MBMV8			MBMV10			MBMV11	
x [cm]	Lx/Lx	Lx/Tx err.	x [cm]	Lx/Lx	Lx/Tx err.	x [cm]	Lx/Lx	Lx/Tx err.	x [cm]	Lx/Lx	Lx/Tx err.	x [cm]	Lx/Lx	Lx/Tx err.	x [cm]	Lx/Lx	Lx/Tx err.
1.6	0.00	0.000	1.3	0.00	0.000	2.3	0.01	0.000	1.5	0.31	0.007	2.4	0.42	0.009	2.2	0.00	0.000
2.6	0.01	0.000	2.4	0.00	0.000	3.3	0.11	0.002	2.8	0.62	0.013	3.6	0.76	0.016	3.3	0.01	0.000
3.6	0.34	0.007	3.4	0.00	0.000	4.4	0.99	0.021	3.9	0.92	0.020	4.7	1.05	0.022	4.2	0.27	0.006
4.7	0.60	0.013	4.5	0.04	0.001	5.4	1.06	0.023	5.0	1.04	0.022	5.6	0.91	0.019	5.2	0.62	0.013
5.7	0.86	0.018	5.5	0.15	0.003	6.4	1.06	0.022	6.1	0.96	0.020	6.7	1.05	0.022	6.1	0.86	0.019
6.7	0.92	0.020	6.5	0.70	0.015	7.4	1.03	0.022	7.1	0.99	0.021	7.8	1.12	0.024	7.1	1.05	0.022
7.7	1.04	0.022	7.5	0.91	0.019	8.4	0.95	0.020	8.2	1.00	0.021	8.7	0.88	0.019	8.0	0.97	0.021
8.6	0.97	0.021	8.5	0.92	0.020	9.3	0.94	0.020	9.2	1.08	0.023	9.8	0.98	0.021	9.0	0.80	0.017
9.5	0.97	0.021	9.5	0.99	0.021	10.3	0.95	0.020	10.3	1.10	0.023	10.9	1.14	0.024	9.9	0.93	0.020
10.4	1.00	0.021	10.5	1.01	0.021	11.4	0.92	0.020	11.4	1.12	0.024	11.9	0.96	0.020	10.8	0.89	0.019
11.4	1.05	0.022	11.5	1.03	0.022	12.4	0.94	0.020	12.4	1.01	0.021	13.0	0.93	0.020	11.8	0.84	0.018
12.4	1.12	0.024	12.5	1.13	0.024										12.7	0.88	0.019
13.5	0.95	0.020	13.5	1.10	0.023	1.7	0.01	0.000	2.0	0.39	0.008	3.1	0.80	0.017			
14.5	0.98	0.021	14.5	1.03	0.022	2.8	0.03	0.001	3.0	0.96	0.020	4.2	0.96	0.020	2.1	0.10	0.002
15.4	1.01	0.021				3.7	0.42	0.009	4.0	0.89	0.037	5.3	1.06	0.023	3.2	0.80	0.017
16.4	0.98	0.021	2.4	0.01	0.000	4.5	0.79	0.017	7.0	1.05	0.022	6.4	1.10	0.023	4.2	0.82	0.018
17.6	0.94	0.020	3.3	0.02	0.000	5.5	0.84	0.018	8.0	0.95	0.020	7.4	0.97	0.021	5.1	0.88	0.019
			4.4	0.12	0.002	6.5	0.97	0.021	9.0	1.04	0.022	8.4	0.94	0.020	6.1	1.04	0.022
1.7	0.01	0.000	5.4	0.45	0.009	7.5	1.15	0.024	10.1	1.15	0.024	9.4	0.91	0.019	7.0	0.96	0.021
2.8	0.01	0.000	6.4	0.75	0.016	8.6	0.94	0.020	11.1	1.07	0.023	10.6	0.98	0.021	8.0	0.99	0.021
3.8	0.05	0.001	7.4	0.88	0.019	9.6	1.08	0.023	12.2	0.91	0.019	11.7	0.87	0.018	8.9	0.92	0.020
4.8	0.34	0.007	8.4	1.10	0.023	10.7	1.12	0.024	13.2	1.01	0.021	12.7	1.04	0.022	9.8	0.98	0.021
5.8	0.64	0.014	9.4	1.06	0.022	11.8	0.97	0.021				13.7	1.04	0.022	11.7	0.92	0.020
6.8	0.97	0.021	10.4	0.92	0.020				1.8	0.85	0.018				12.7	0.91	0.020
7.8	1.02	0.022	11.4	0.96	0.020	1.6	0.00	0.000	2.9	0.93	0.020	1.8	0.02	0.000			
8.9	0.94	0.020	12.4	0.86	0.018	2.8	0.04	0.001	4.2	1.01	0.022	3.1	0.23	0.005	1.8	0.01	0.000
10.0	1.07	0.023	13.4	0.90	0.019	3.8	0.42	0.009	5.4	0.90	0.019	4.2	0.73	0.015	2.8	0.21	0.005
			14.3	1.09	0.023	4.8	0.95	0.020	6.6	0.94	0.020	5.3	1.09	0.023	3.8	0.60	0.013
2.3	0.03	0.001	15.2	1.09	0.023	5.9	1.06	0.022	7.6	1.06	0.023	6.4	0.93	0.020	4.7	0.86	0.018
3.4	0.21	0.005				6.9	1.08	0.023	8.6	0.93	0.020	7.4	1.00	0.021	5.7	0.96	0.021
4.4	0.66	0.014	1.4	0.01	0.000	8.0	0.92	0.020	9.7	1.00	0.021	8.5	0.93	0.020	6.7	0.97	0.021
5.4	0.86	0.018	2.2	0.01	0.000	8.9	1.07	0.023	10.7	1.06	0.023	9.7	1.07	0.023	7.7	0.90	0.019
6.4	0.96	0.020	3.0	0.15	0.003	10.0	0.94	0.020	12.1	1.04	0.022	10.8	0.96	0.021	8.7	0.94	0.020
7.3	1.08	0.023	3.9	0.31	0.007	11.3	0.94	0.020	13.4	0.84	0.018				9.6	1.04	0.022
8.3	1.01	0.021	4.7	0.70	0.015	12.4	1.00	0.021							10.6	1.21	0.026
9.2	1.10	0.023	6.3	0.93	0.020										11.5	1.00	0.021
10.2	1.00	0.021	7.1	0.82	0.017										12.4	0.93	0.020
11.2	0.96	0.020	7.9	0.89	0.019												
12.3	0.88	0.019	8.6	0.89	0.019										1.9	0.03	0.001
13.2	0.88	0.019	9.4	0.79	0.017										3.2	0.15	0.003
14.2	0.97	0.021													4.1	0.53	0.011
15.2	0.90	0.019													5.1	0.99	0.021
															6.1	1.05	0.022
															7.0	1.1	0.024
															7.9	1.2	0.026
															8.8	1.0	0.022
															9.8	1.1	0.024
															10.7	1.2	0.026
															11.6	1.1	0.024
															12.6	0.9	0.019

746
747
748

749 **Table A3:** Best-fit values of $\overline{\sigma\varphi}_0$ and μ determined for each sample, calculated from combinations of

750 three and four samples.

Calibration combination				$\overline{\sigma\varphi}_0$ [s^{-1}]			μ [mm^{-1}]		
				Best-fit	+1σ	-1σ	Best-fit	+1σ	-1σ
with 3 samples, MBMV...									
1	7	8		1.2 10^{-7}	1.2 10^{-7}	1.1 10^{-7}	1.51	1.52	1.50
1	7	10		6.6 10^{-8}	7.6 10^{-8}	6.4 10^{-8}	1.42	1.43	1.38
1	7	11		9.4 10^{-8}	9.6 10^{-8}	7.8 10^{-8}	1.42	1.45	1.39
1	8	11		7.4 10^{-8}	7.5 10^{-8}	6.1 10^{-8}	1.39	1.39	1.34
1	8	10		1.0 10^{-7}	1.0 10^{-7}	1.0 10^{-7}	1.42	1.43	1.41
1	10	11		6.6 10^{-8}	8.3 10^{-8}	6.0 10^{-8}	1.39	1.39	1.33
7	8	10		1.3 10^{-7}	1.3 10^{-7}	1.3 10^{-7}	1.58	1.58	1.56
7	8	11		1.2 10^{-7}	1.2 10^{-7}	1.2 10^{-7}	1.51	1.52	1.50
7	10	11		1.4 10^{-7}	1.5 10^{-7}	1.3 10^{-7}	1.58	1.60	1.55
8	10	11		8.1 10^{-8}	9.1 10^{-8}	7.3 10^{-8}	1.34	1.37	1.31
with 4 samples, MBMV…									
1	7	8	10	9.5 10^{-8}	9.9 10^{-8}	8.5 10^{-8}	1.48	1.48	1.45
1	7	8	11	1.1 10^{-7}	1.1 10^{-7}	1.1 10^{-7}	1.48	1.49	1.47
1	7	10	11	7.4 10^{-8}	8.1 10^{-8}	6.5 10^{-8}	1.38	1.41	1.36
1	8	11	10	9.0 10^{-8}	9.4 10^{-8}	8.7 10^{-8}	1.42	1.42	1.40
7	10	11	8	1.2 10^{-7}	1.2 10^{-7}	1.2 10^{-7}	1.53	1.53	1.52

751

29

752

753 **Table A4:** Inversion results for exposure age using the different calibration combinations of bedrock

754 samples. Grey shading shows the inverted results for a specific sample when not included in the

755 calibration combination (i.e. the exposure age of the specific sample has not used for the calibration of

756 the model). These results are used to produce Figures 10c-d.

757

Calibration combination				MBMV1 - 137 yrs				MBMV7 - 69 yrs				MBMV8 - 3 yrs				MBMV10 - 18 yrs				MBMV11 - 30 yrs			
				Best fit	Median	+2 σ	-2 σ	Best fit	Median	+2 σ	-2 σ	Best fit	Median	+2 σ	-2 σ	Best fit	Median	+2 σ	-2 σ	Best fit	Median	+2 σ	-2 σ
Individually				146	152	172	126	89	79	88	67	2	3	3	2	19	19	23	14	50	42	50	34
with all the sample excluding MBMV6				164	161	185	132	61	63	68	57	3	3	4	3	17	14	18	9	62	57	70	41
with 3 samples, MBM V...																							
1	7	8		184	166	190	136	56	62	67	56	3	3	3	2	9	13	17	9	53	54	69	40
1	7	10		194	183	213	146	77	80	88	71	5	5	5	4	21	18	23	13	90	69	88	50
1	7	11		118	126	149	103	56	56	61	50	3	3	4	3	15	12	16	9	57	50	61	35
1	8	11		122	135	159	104	61	63	70	56	3	4	4	3	13	15	18	10	55	53	68	39
1	8	10		106	113	134	92	50	50	55	45	3	3	3	2	14	12	15	8	50	43	55	31
1	10	11		174	150	181	119	67	71	80	63	4	4	5	4	17	17	21	12	44	61	77	44
7	8	10		181	211	242	173	78	74	82	64	3	3	3	2	16	13	17	9	78	65	78	48
7	8	11		165	162	189	136	66	62	67	56	3	3	3	2	14	13	17	9	40	54	68	40
7	10	11		206	189	216	155	65	65	73	57	3	3	3	2	15	12	15	8	65	58	70	43
8	10	11		116	93	116	71	46	50	55	43	3	3	4	3	11	12	15	9	52	42	52	29
with 4 samples, MBMV ...																							
1	7	8	10	176	170	194	139	63	67	73	61	4	4	4	3	10	15	19	10	68	61	75	43
1	7	8	11	177	152	174	125	63	59	64	54	3	3	3	3	15	13	17	9	63	52	66	38
1	7	10	11	129	129	154	98	58	62	69	54	4	4	4	3	13	14	18	10	38	52	66	38
1	8	11	10	117	134	155	106	58	58	64	52	4	3	4	3	16	13	17	9	42	52	64	36
7	10	11	8	159	168	196	141	63	63	69	56	2	3	3	2	16	13	16	9	52	55	69	41

758
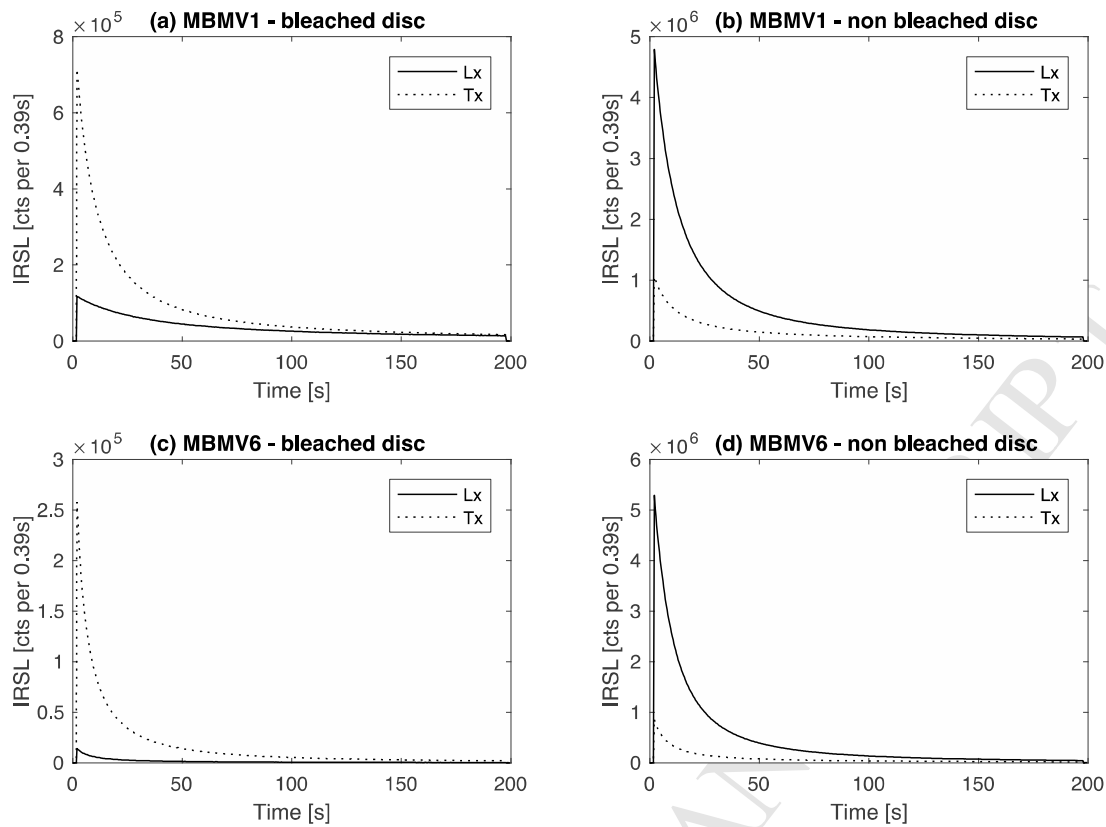
Figure A3: Natural infrared stimulated signal (solid line, Lx) and test dose (27.25 Gy) subsequent luminescence response (dashed line, Tx) for a bleached signal (surface disc) (a) and (b) and for non-bleached signal (inside core disc) (b) and (c). (a) and (b) are IRSL signal representative for gneissic lithology (sample MBMV1). (c) and (d) for granitic lithology (sample MBMV6).

References

G.E. King, F. Herman and B. Guralnik, 2016. Northward migration of the eastern Himalayan syntax revealed by OSL-thermochronometry. Science 353 (6301), 800-804.

Sohbati, R., Jain, M., Murray, A., 2012a. Surface exposure dating of non-terrestrial bodies using optically stimulated luminescence: A new method. Icarus 221, 160-166.